Quantifying the intricacies of biological pattern formation: A new perspective through complexity measures

Jurgen Riedel*, Chris P. Barnes

Department of Cell and Developmental Biology, University College London, London, United Kingdom

Abstract

In this study we examine the emergence of complex biological patterns through the lens of reaction-diffusion systems. We introduce two novel complexity metrics — Diversity of Number of States (DNOS) and Diversity of Pattern Complexity (DPC)— which aim to quantify structural intricacies in pattern formation, enhancing traditional linear stability analysis methods. We demonstrate this approach to different systems including the linear Turing, Gray-Scott and FitzHugh-Nagumo models. These measures reveal insights into nonlinear dynamics, multistability, and the conditions under which complex biological patterns stabilize. We then apply the approach to gene regulatory networks, including models of the toggle switch in developmental biology, demonstrating how diffusion and self-activation contribute to robust spatial patterning. Additionally, simulations of the Notch-Delta-EGF signaling pathway in Drosophila neurogenesis highlight the role of gene regulation and parameter variations in modulating pattern complexity and state diversity. Overall, this work establishes complexity-based approaches as valuable tools for exploring the conditions that drive diverse and stable biological pattern formation, offering a pathway for future applications in synthetic biology and tissue engineering.

1 Introduction

Research has long focused on understanding how structure and order arise in biological systems, a quest dating back to Aristotle's "History of Animals". A critical component of this exploration is understanding the mechanisms behind pattern formation during embryonic development, essential for elucidating the evolution of multicellular organisms from single fertilized cells. This complex process, characterized by the development of intricate spatial features with exceptional precision and robustness, encompasses a wide range of mechanisms.

Foundational models for studying embryogenesis and pattern formation use reaction–diffusion equations Maini [2004]. This approach was first introduced by Turing[Turing, 1952] and further developed by Gierer and Meinhardt [Gierer and Meinhardt, 1972]. The

Turing model, at its core, is a mathematical framework that explores how reaction-diffusion systems can lead to pattern formation, Turing patterns (TP). The typical formulation of a Turing model comprises two or more interacting chemical species that diffuse and react within a spatial domain. The dynamics of the concentrations of these species are governed by a set of partial differential equations (PDEs). TP models have been used to explain diverse animal coat markings [Staddon, 2024], [Kondo et al., 2021], effectively describing cell interactions [Nakamasu et al., 2009], [Jahanbakhsh and Milinkovitch, 2022] and the impact of organism geometry on pattern manifestation[Maini and Woolley, 2019], [Alessio and Gupta, 2023]. However, they face challenges in scaling with growth [Diez et al., 2023, Werner et al., 2015], integrating detailed biological data [Benenson, 2012, Tanaka et al., 2023, Volkening, 2024], and adapting to specific biological scenarios [Kondo, 2017, Krause and Gaffney, 2021, Rietkerk et al., 2021], necessitating ongoing refinements to enhance their applicability and accuracy [Milinkovitch et al., 2023].

Analysis of TP models normally proceeds through linear stability analysis and bifurcation, methods from dynamical systems theory Maini [2004]. This approach allows one to find parameters that give rise to instabilities, which are an indicator of pattern forming potential. These approaches have been successful in showing system properties. For example, traditionally, TPs were generally understood to lack robustness, meaning slight variations in model parameters and structure can significantly influence their behavior and stability Schnoerr et al. [2020], Woolley et al. [2021]. This was exemplified by stringent requirements for diffusion rates and reaction parameters for instability and pattern formation. However, recent computational studies reveal that networks with relaxed diffusion constraints are more prevalent than previously understood, suggesting that Turing patterns are more likely and robust in natural systems than once thought [Marcon et al., 2016, Diego et al., 2018]. In another study, an extensive analysis of thousands of networks showed that many can generate Turing patterns, highlighting their common occurrence in biological systems and likelihood of arising through evolution, but the stability of these patterns can still be sensitive to small changes in network parameter values[Scholes et al., 2019]. Actual biological systems exhibit a dynamic equilibrium between stabilizing biochemical reactions and destabilizing molecular diffusion within more complex gene regulatory networks, and this underlies how cells interpret morphogen signals to make robust developmental decisions, even amidst significant environmental and evolutionary changes [Roy et al., 2023, Dalwadi and Pearce, 2023]. Understanding these deeper results has spearheaded engineering biology efforts to elucidate the biological processes underlying robust pattern formation [Scholes et al., 2019, Vittadello et al., 2020, Tica et al., 2023].

The limitations of linear stability analysis in predicting the long-term persistence of patterns in reaction-diffusion systems have been highlighted in recent research [Klika, 2017],[**?**],[Krause, 2024]. While this analysis is essential for identifying potential instabilities that can lead to pattern formation, it only provides a local view of the system's behavior. Findings reveal that even when instability conditions are met, resulting patterns may be transient, especially in systems characterized by mild multi-stable nonlinearities Krause [2024]. This observation is crucial in contexts such as gene regulatory networks and spatial ecosystems, where the presence of multiple stable homogeneous equilibria often leads systems to revert to a stable, unpatterned state after an initial period of transient patterning Krause [2024]. A novel approach incorporating non-linear terms enhances the predictive power of Turing pattern

formation analysis by providing analytical, approximate solutions for pattern amplitudes has been proposed Chen and Buceta [2019]. This method bridges the gap between linear predictions and long-term behavior, improving understanding of conditions for stable pattern formation and highlighting the role of non-linear dynamics in predicting pattern amplitude and stability, especially in complex, multi-stable systems.

Despite advancements in methods for analyzing pattern formation, limitations persist, especially in systems with multistability, strong nonlinearities, and far-from-equilibrium dynamics [Aragón et al., 2012], [Huidobro and Endres, 2024], [Pazuki and Endres, 2024]. Expansion techniques, such as amplitude equations, often break down beyond bifurcation points, neglecting higher-order nonlinearities that can significantly alter pattern stability. These methods also fail to account for transient patterning in multistable systems, where patterns may decay to homogeneous states. Additionally, they struggle with the complexity of high-dimensional systems, where interactions among many components exceed their computational scope. Most approaches are deterministic and overlook stochastic effects, which are critical in real-world biological and ecological systems. While these methods improve upon classical linear stability theory, they offer limited predictive power for long-term dynamics and far-from-equilibrium behaviors, necessitating more robust analytical tools.

Complexity-based approaches offer a robust and comprehensive framework for analyzing pattern formation, extending beyond the limitations of traditional linear methods by encompassing both linear and nonlinear dynamics. These methods allow for the measurement of various facets of patterns, such as structural intricacy and state diversity, resulting in a multidimensional assessment that goes beyond simple spatial characteristics. For instance, complexity metrics, by integrating nonlinear interactions, are able to capture the richness and variability of biological patterns, which is critical for facilitating comparative analyses across diverse models and enhancing our understanding of the underlying biological mechanisms [Paul et al., 2023], [van der Kolk et al., 2023].

Furthermore, the scalability and broad applicability of complexity-based metrics make them especially well-suited for the analysis of large and intricate systems. In gene regulatory networks, these measures help bridge the gap between theoretical predictions and empirical observations by quantifying the nonlinear feedback loops and emergent behaviors that are central to biological processes [Subbaroyan et al., 2022]. Complexity measures not only overcome the limitations inherent in linear methods but also provide deeper insights into the multifaceted nature of pattern formation, including the emergence of geometric Turing patterns and the cybernetic nature of gene networks, which are critical for understanding developmental biology and system robustness [Hagolani et al., 2023, Forestiero, 2022]. Thus, complexity-based approaches serve as powerful tools for advancing the study of complex biological systems.

However, some key questions remain. Given a system is unstable, and undergoes pattern generation, what is the nature of the resulting pattern? Can we quantify the complexity of pattern formation? These are the questions we consider in this work.

This paper is structured as follows. We first outline the basics of the Turing model and how it is treated with traditional linear stability analysis. We then outline new complexity-based measures that can provide insight into the resultant patterns formed from the reaction-diffusion system. We then apply this new approach to systems of increasing complexity, demonstrating how these measures can quantity pattern formation. We also outline a scheme

for classifying pattern forming systems based on these complexity measures.

2 Results

2.1 Stability analysis of the linear Turing model

The Turing model, at its core, is a mathematical framework that explores how reaction-diffusion systems can lead to pattern formation. The typical formulation of a Turing model comprises two or more interacting chemical species that diffuse and react within a spatial domain. The dynamics of the concentrations of these species are governed by a set of partial differential equations (PDEs), reflecting Turing's initial presentation of the concept Turing [1952]. A simplified presentation of a two-species Turing model is defined by the partial differential equations:

$$\frac{\partial u}{\partial t} = D_u \nabla^2 u + f(u, v), \tag{1}$$

$$\frac{\partial v}{\partial t} = D_v \nabla^2 v + g(u, v), \tag{2}$$

where u and v are the concentrations of two chemical species (activator and inhibitor, respectively), D_u and D_v their diffusion coefficients, ∇^2 the Laplacian operator indicating spatial diffusion, $f(u, v)$ and $g(u, v)$ the reaction kinetics functions, and t time. For TPs to emerge, the activator promotes its own production as well as the production of the inhibitor, while the inhibitor suppresses the production of the activator. This interplay between local activation and lateral inhibition, combined with differential diffusion rates, facilitates the emergence of spatial patterns.

We can simplify further by linearisation of the interaction functions $f(u, v)$ and $g(u, v)$. This approach offers a tractable toy model while retaining the essence of pattern formation in reaction-diffusion processes:

$$\frac{\partial u}{\partial t} = a(u - h) + b(v - k) + D_u \nabla^2 u, \tag{3}$$

$$\frac{\partial v}{\partial t} = c(u - h) + d(v - k) + D_v \nabla^2 v. \tag{4}$$

where $f(u, v) = a(u - h) + b(v - k)$ and $g(u, v) = c(u - h) + d(v - k)$ describe the linear dynamics of the state variables u and v. Parameters a and d are the self-feedback rates for the activator u and the inhibitor v, respectively, influencing how their concentrations evolve, b and c are the cross-interaction coefficients, with b indicating how the inhibitor v affects the activator u, and c showing the impact of the activator u on the inhibitor v. As above, D_u and D_v are the diffusion coefficients for the activator and inhibitor, dictating their dispersion in the spatial domain. Parameters h and k represent the baseline or equilibrium concentrations of u and v, around which the system's linearized reaction functions are centered.

In reaction-diffusion systems, instability catalyzes pattern formation by amplifying minor perturbations through differential diffusion rates, leading to complex pattern emergence. Conversely, stability, marked by negative real parts of all eigenvalues in linearized equations,

suppresses pattern formation by maintaining homogeneity. Turing's paradoxical finding that diffusion can induce instability under significant activator-inhibitor diffusion rate disparities has profound implications across biology and materials science, enabling the spontaneous emergence of patterns such as stripes or spots Turing [1952], Maini and Woolley [2019].

We applied stability analysis to the the linear Turing model using standard approaches (see Methods) to identify stable fixed points (both eigenvalues negative) and instability (at least one positive eigenvalue) and saddle points (eigenvalues of opposite signs). Bifurcations, including transcritical, pitchfork, and Hopf, are identified by eigenvalue behaviors. The diffusion coefficients D_u and D_v are pivotal in system dynamics, influencing pattern stability and emergence. Both D_u and D_v were varied within 1×10^{-5} to 1×10^{-3}. The reaction parameters a, b, c, and d were varied over the interval $[-2, 2]$ and the wave number k varied from 0 to 100. This methodical approach delineates the parameter space for understanding Turing pattern emergence in reaction-diffusion systems.

Figure 1 shows a summary of the dynamical properties over the (D_u, D_v) plane. The variation in colors (from low, red, to high, blue) across the D_u and D_v space indicates the density of stable (1A) and saddle points (1B), pitchfork (1C), transactional bifurcations (1D) and Hoft bifurcations (1E), and the average pattern length scale (1F). Stability dictates the system's response to perturbations. Different bifurcation types indicate transitions in system behavior. Length scale approach not only forecasts pattern emergence, such as stripes or spots, but also clarifies their size and spacing by analyzing the impact of system parameters.

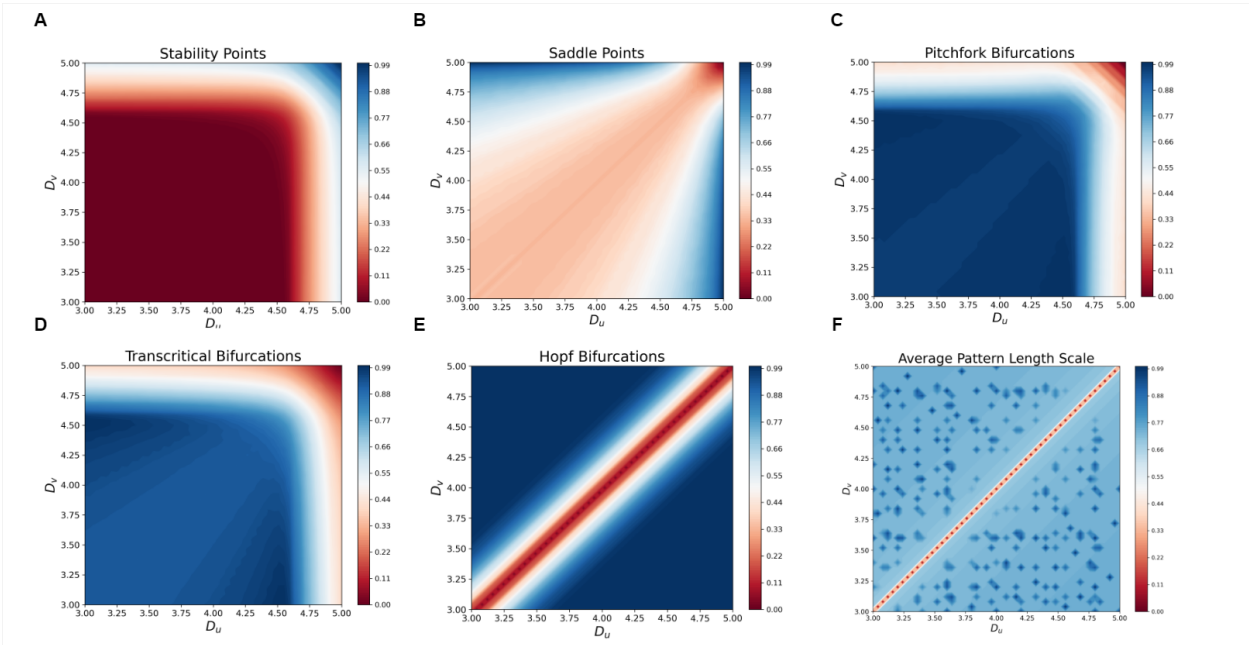

Figure 1: Stability analysis of the linear Turing model. The variation in colors across the D_u and D_v space indicates the density of stable points (A), saddle points (B), pitchfork bifurcations (C), transcritical bifurcations (D), Hopf bifurcations (E), and the average pattern length scale (F). Darker regions suggest higher density of points, while lighter regions indicate lower density.

2.2 Development of new complexity measures

This section introduces a novel approach to analyzing pattern formation through a coarse-grained perspective of the continuous system, aiming not just to bridge the gap between linear stability analysis and actual pattern behaviour but to develop a holistic understanding of pattern formation. We propose two mathematical measures: the Diversity of Number of States (DNOS) and the Diversity of Pattern Complexity (DPC) to offer a methodology for evaluating the complexity within continuous systems to shed further light on pattern formation dynamics. Figure 2 gives an overview of how these are calculated. A mathematical defintion of these two measures is provided in (Methods 4.1.1).

The calculation of DNOS begins with the binning of the output from the computational model, represented as a pixel grid (by default we use an 80x80 grid) where each pixel value denotes the concentration of a reactant within the spatial domain at a particular time (2C). Each bin represents a specific range of state values. For instance, if the interval [0, 1] is divided into ten bins, each bin spans a range of 0.1 units. Each state value within the pixel grid is then discretized. For example, a state value of 0.013 falls into the [0.0-0.1) bin, while a value of 0.34 falls into the [0.3-0.4) bin (2D). This mapping is systematically applied to all state values, resulting in a transformed matrix where each entry corresponds to a discrete bin identifier. Subsequently, a set S is constructed, containing all unique bin identifiers that appear in the discretized state matrix. This set represents the distinct intervals occupied by the reactant concentrations across the entire grid at a given time t. The DNOS is then defined as the cardinality of this set S, effectively counting the number of unique bins occupied by the state values.

This measure provides a quantitative assessment of the complexity and diversity of the reactant concentration distribution. For instance, considering state values such as 0.013, 0.028, 0.34, 0.36, 0.427, 0.546, 0.572, 0.689, and 0.896, the corresponding bins might be [2], [3], [4], [5], [6], [8], and [9]. Thus, the DNOS would be 7, indicating that the state values span seven distinct intervals (2D).

The second measure, DPC, leverages lossless compression to quantify the complexity of patterns in a reaction-diffusion system. Starting with the same pixel grid as defined for DNOS, the model output is converted into an RGB image. This conversion allows for a clear representation of the spatial distribution of reactant concentrations. Following this, the RGB image undergoes a lossless compression process using the gzip algorithm (2A). The complexity of each pattern is then quantified by calculating the compression ratio (CR), defined as the size of the compressed image divided by the size of the uncompressed image.

Each compression ratio is systematically mapped to its corresponding bin. For instance, a compression ratio of 0.17 falls into the [0.1-0.2) bin, whereas a ratio of 0.35 falls into the [0.3-0.4) bin (2B). This mapping results in a transformed dataset where each compression ratio is categorized into discrete intervals. To construct the DPC, a set S is formed containing all unique bin identifiers that appear across the compression ratios of observed patterns.

Additionally, we introduce the Uniformity Measure of Entropy (UME) (Section 4.1.2) as a complementary metric to both DNOS and DPC. UME quantifies the uniformity of a distribution of values within a system, providing insight into how evenly those values are spread across their respective bins. Applied to both compression ratios (UME(CR)) and state values (UME(S)), UME scales and discretizes the data into specific bins and then computes the

Shannon entropy of the distribution. The entropy is normalized by the maximum possible entropy, resulting in a measure ranging from 0 to 1, where 1 indicates a perfectly uniform distribution and values closer to 0 indicate greater unevenness. UME(CR) extends the analysis of pattern complexity by reflecting how evenly compression ratios are distributed across complexity levels, offering a uniformity perspective on DPC. Similarly, UME(S) quantifies the uniformity of state distributions, complementing DNOS by capturing how evenly state values are distributed across spatial regions of the reaction-diffusion system. This allows for a richer understanding of pattern formation dynamics, combining both diversity and uniformity aspects of the system's complexity.

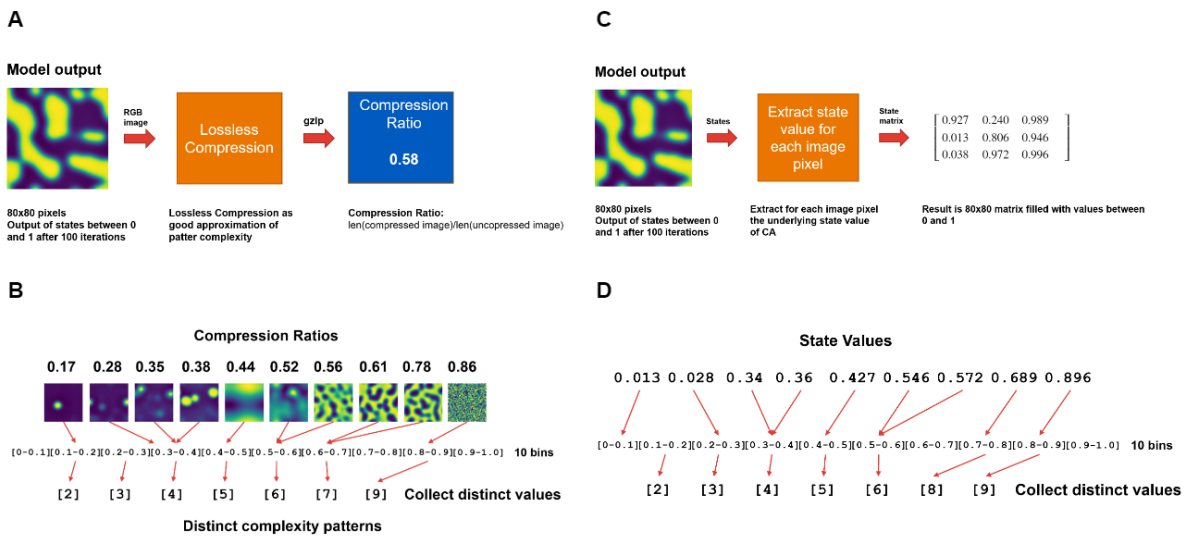

Figure 2: Development of new complexity measures. **A:** The methodology for constructing the Discrete Number of States (DNOS) in a reaction-diffusion system starts with a computational model output at time, t, shown as an 80x80 pixel grid, where each pixel represents reactant concentration with values from 0 to 1. These continuous values are discretized into bins, e.g., the interval [0, 1] into ten bins of 0.1 units each, transforming state values into discrete categories. **B:** State values are mapped to bins, e.g., 0.013 to [0.0-0.1) and 0.34 to [0.3-0.4), creating a matrix of bin identifiers. A set S of unique bins is formed, representing the distinct intervals occupied by the reactant concentrations at time t. DNOS is the count of unique bins, indicating the complexity and diversity of the distribution. For instance, values such as 0.013, 0.34, and 0.896 span bins [2], [4], and [9], leading to a DNOS of 7. **C:** Constructing Discrete Pattern Complexity (DPC) involves using lossless compression to quantify pattern complexity in a reaction-diffusion system. The model output is converted into an RGB image, which is then compressed using the gzip algorithm. The compression ratio (CR) is calculated as the size of the compressed image divided by the uncompressed image size. **D:** A compression ratio of 0.58 illustrates pattern complexity. Various patterns at different time points yield ratios such as 0.17, 0.28, and 0.35. These ratios are discretized into bins (e.g., [0.0-0.1), [0.1-0.2)), and each ratio is mapped to its bin, transforming the data into discrete intervals. DPC is defined as the number of unique compression ratios, quantifying the diversity of pattern complexities.

2.3 Exploring the complexity space of the linear Turing model

In this section we numerically solve the PDE system using the finite-difference method (Section 4.2) and revisit the linear Turing model by exploring a comprehensive range of diffusion and reaction parameters to investigate their impact on pattern formation in two-dimensional concentration fields. The parameters and their respective ranges are shown in (Table 1).

Parameter	Description	Range	Increment
D_u **(log scale)**	Diffusion rate of u	10^{-3} to 10^{-5}	0.2 (logarithmic)
D_v **(log scale)**	Diffusion rate of v	10^{-3} to 10^{-5}	0.2 (logarithmic)
a	Reaction rate for u	-2 to 2	0.2
b	Interaction of v with u	-2 to 2	0.2
c	Reaction rate for u	-2 to 2	0.2
d	Reaction rate for v	-2 to 2	0.2
dx	Spatial resolution	Computed as 1/SIZE	
dt	Time step	0.02	

Table 1: Summary of the parameters and their ranges explored in the simulation.

In our analysis, we focus on the simulation outputs after 10^3 time steps for all combinations of diffusion coefficients D_u and D_v and the parameters a, b, c, and d. To compute the Distinct Pattern Count (DPC) for each D_u, D_v pair, we first calculate the compression ratios of the u field outputs across all permutations of the reaction parameters a, b, c, and d. Subsequently, we discretize the floating-point values of the DPC to four decimal places and enumerate all unique values to determine the DPC for each D_u, D_v pair. For the Distinct Number of States (DNOS) associated with each D_u, D_v pair, we discretize the floating-point values of the u field to four decimal places for every combination of a, b, c, and d, and count all unique values. By averaging these DNOS values over all parameter combinations, we derive the DNOS for each D_u, D_v pair (see Methods).

We analyzed this type of segmentation further and we plot all normalized DPC and DNOS values for all D_u, D_v pairs in the plane (Figure 3C-F). The data points of the reaction-diffusion system are clustered using the KMeans algorithm, identifying distinct clusters and calculating centroids as the mean position of all points in each cluster. In order to show the effect on bin size we are considering 10^3 bins (Figure 3C) and into 10^4 bins (Figure 3D). Both plots show that the values form four distinct clusters. More specifically, if one imagines the plane to be sectioned into quadrants, one cluster (1) is located in the lower left quadrant with low DPC and DNOS values. Another cluster (2) is located in the top left quadrant having low DPC values but high DNOS values. The third clusters (0) are located in the top right quadrant with both having high DPC and DNOS values. However, a bin size 10^3 shows the data points of each cluster smeared across the DPC axis whereas the data points in each cluster for bin size 10^4 are more localized.

In order to aim for a better cluster separation, especially cluster 0 appears to be split into two sub clusters, we employ the Uniformity Measure of Entropy (UME) (Section 4.1.2) to examine the DPC and DNOS bins. By scaling from 0 (highly concentrated) to 1 (perfectly uniform), this measure refines the separation of data distributions that are typically focused on sections of nearby bins, allowing for a more detailed differentiation between various DPC and DNOS configurations across the reaction-diffusion model outputs. The application of UME to the the DCP and DNOS values before the clustering results in four well separated clusters for bin size 10^3 and bin size 10^4 (Figure 3E-F). In particular, the top right corner we have two well separated clusters (0 and 3).

Figure 3 A,B show contour plots of normalized DPC and DNOS values with UME over the D_u, D_v plane respectively. Both plots show segmentation into distinct quadrants, which is more clearly visible in the DPC plot than the DNOS plot. In the DPC plot, the lower

left quadrant ($10^{-4} > D_u < 10^{-3}$ and $10^{-4} > D_v < 10^{-3}$) and the upper right quadrant ($10^{-5} > D_u < 10^{-4}$ and $10^{-5} > D_v < 10^{-4}$) have the lowest values, while the upper left quadrant ($10^{-4} > D_u < 10^{-3}$ and $10^{-5} > D_v < 10^{-4}$) has the highest values, and the lower right quadrant ($10^{-5} > D_u < 10^{-4}$ and $10^{-4} > D_v < 10^{-3}$) values fall in between.

We are now relate the clusters of the D_u-D_v plane to the contour plots of normalized DPC and DNOS. relate this result to the first two plots, we map each cluster's data points back to the parameter space D_v over D_u (Figure 3G). In this plot, we see that the clusters map neatly into the four parameter quadrants as discussed earlier. On the diagonal, we find clusters 1 and 2, whereas the other clusters 0 and 3 are on the off diagonal.

For each cluster around the centroids, data associated with the diffusion parameters D_u and D_v were extracted to analyze state variables under different conditions. Feature vectors and state space vectors were scaled, discretized, and analyzed to identify predominant patterns. The mode value, representing the most frequent occurrence within each bin, was used to select the sample from each bin. Images were created from this data and the DPC values were calculated. These images were sorted by complexity, and 20 representative samples were selected from n bins using an equal distance sampling method. The images were displayed in a grid format, organized by cluster and sorted by complexity, to provide insights into the system's dynamic patterns (Figure 3H). Cluster 1, having low DPC and DNOS values, exhibits the least pattern diversity. Cluster 2, having low DCP but high DNOS values, shows a higher degree of pattern diversity. In contrast, clusters 0, having high DCP and DNOS values, display high patter diversity and cluster 3, having the highest DCP and DNOS values of all, displays pattern diversity that is similar high but also shows the most variance of pattern scales.

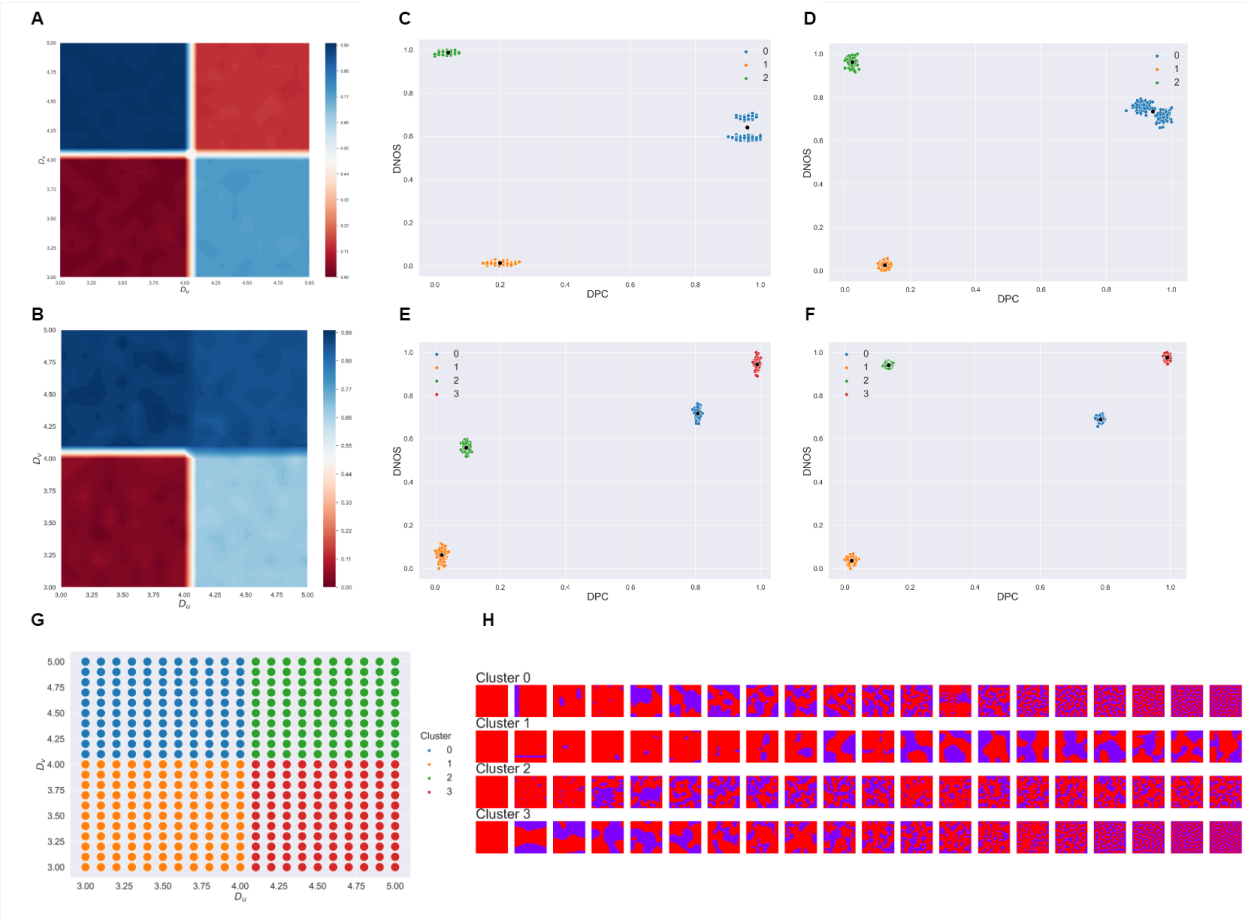

Figure 3: Exploring the complexity space of the linear Turing model. **A,B:** Discretizing pattern complexity into 10^4 bins, showing a contour plot of normalized DPC and DNOS values over $D_u \times D_v$. **C-F:** Normalized DPC and DNOS values for all D_u and D_v pairs in a plane. Data points of the reaction-diffusion system were clustered using the KMeans algorithm, identifying distinct clusters and calculating centroids as the mean position of all points in each cluster. **C,D:** Discretizing pattern complexity and number of states values into 10^3 bins as shown in C and into 10^4 bins as shown in D, showing a scatter plot of normalized DPC and DNOS values for all D_u and D_v pairs in a plane DPC over $DNOS$., **E,F:** Same setup as in C,D but now applying Uniformity Measure of Entropy to calculate DPC and $DNOS$. **E:** showing results for values discretized into 10^3 bins and **F:** into 10^4 bins., **G:** , showing a scatter plot mapping the clusters from **F**(discretizing pattern complexity and number of states values into 10^4 bins) onto all D_u and D_v pairs in the plane DPC over $DNOS$., **H:** For each cluster around the centroids, data associated with the diffusion parameters D_u and D_v were extracted to analyze state variables under different conditions. Feature vectors and state space vectors were scaled, discretized, and analyzed to identify predominant patterns. The mode value, representing the most frequent occurrence within each bin, was used to select the sample from each bin. Images were created from this data and the DPC values were calculated. These images were sorted by complexity, and 20 representative samples were selected from n bins using an equal distance sampling method. The images were displayed in a grid format, organized by cluster and sorted by complexity, to provide insights into the system's dynamic patterns.

2.4 The Gray-Scott model

The Gray-Scott model involves two chemical species that diffuse at different rates, resulting in complex, stationary spatial patterns governed by nonlinear partial differential equations. Studies by Doelman, Gardner, and Kaper (1997, 1998) have explored the stability and diverse morphologies of these patterns, highlighting the dynamics driven by the interplay between reaction kinetics and diffusion, which creates stable localized structures McGough and Riley [2004]. Gray and Scott's (1983) analysis of autocatalytic reactions in an isothermal continuous stirred tank reactor (CSTR) revealed phenomena such as multistability, hysteresis, and oscillations, providing critical insights into various stationary states and dynamic behaviors, including isolas and mushrooms in pattern formation Gray and Scott [1983].

Extensive mathematical and computational analyses have clarified the conditions under which these patterns form and persist, making the Gray-Scott model a fundamental framework for understanding pattern formation in chemical, biological, and ecological contexts McGough and Riley [2004]. Practical applications of the model span chemistry, biology, and physics, with high-fidelity numerical simulations capturing a variety of wave patterns, such as stationary and non-stationary waves, pulse-splitting waves, and self-replicating spots M. Zheng and Xu [2020]. The model's ability to generate and analyze complex patterns through reaction kinetics and diffusion has made it invaluable in both theoretical research and practical applications across multiple scientific domains J. Li and Zhang [2019]. By providing profound insights into the mechanisms of pattern formation, the Gray-Scott model continues to be a cornerstone in the study of dynamic systems and their applications McGough and Riley [2004], Gray and Scott [1983], M. Zheng and Xu [2020], J. Li and Zhang [2019].

The mathematical formulation of the Gray-Scott model can be expressed as a set of coupled partial differential equations that describe the spatiotemporal evolution of the chemical species involved. Specifically:

$$\frac{\partial a}{\partial t} = D_a \nabla^2 a + f(a,b), \qquad \frac{\partial b}{\partial t} = D_b \nabla^2 b + g(a,b), \tag{5}$$

$$f(a,b) = -uv^2 + \alpha(1-a), \qquad g(a,b) = ab^2 - (\alpha+\beta)v, \tag{6}$$

where D_a and D_b are diffusion coefficients for u and v respectively, ∇^2 represents the Laplacian operator indicating spatial diffusion, and $f(a,b)$ and $g(a,b)$ define the reaction kinetics in the Gray-Scott model. Here, α and β adjust the activator's feed and inhibitor's removal rates, with $-ab^2$ modeling activator consumption by the inhibitor, $\alpha(1-a)$ the activator feed rate, ab^2 the inhibitor production, and $-(\alpha+\beta)v$ the combined feed and decay rates of the inhibitor.

This representation aligns the Gray-Scott model with the general framework of Turing pattern systems, highlighting the specific interaction functions that drive the dynamics of pattern formation in this model.

Using a similar numerical setup as in (Section 2.3) we collect outputs after 10^2 time steps for all combinations of diffusion coefficients D_u and D_v and the parameters a and b. A complete set of parameters used and their respective ranges are shown in (Table 2).

In Figure 4 A,F show contour plots of normalized DPC and DNOS values over the D_u, D_v plane respectively collecting discretizing values into 10^4 bins. We explore additional

Parameter	Description	Range	Increment
D_u	Diffusion rate of u	0.1 to 0.2	0.005
D_v	Diffusion rate of v	0.01 to 0.1	0.0045
a	Reaction rate for u	0 to 0.01	0.0005
b	Interaction of v with u	0 to 0.01	0.0005
dx	Spatial resolution	1	
dt	Time step	1	

Table 2: Summary of the parameters and their ranges explored in the simulation.

measures of pattern complexity to compare the results with DPC as follows: The spectral energy (ESP) (Methods 4.1.3) measure quantifies the total variance of an image's frequency components, excluding the zero frequency, provides insights into the textural and structural complexity within the image's spatial domain. Concurrently, the wavelet energy ratio (WLE) (Methods 4.1.5), defined as the ratio of the sum of squared detail coefficients to the squared approximation coefficients from a wavelet decomposition, explains the image's complexity by highlighting the relative presence of high-frequency details versus low-frequency approximations, thereby indicating the extent of textural and edge information. Additionally, the resistance distance histogram (RDH) (Methods 4.1.4) of a graph derived from an image captures the distribution of pairwise electrical resistance distances among its nodes, reflecting the image's topological complexity through the variability in connectivity and path redundancy within its underlying structure.

We related these measures by creating additional contour plots of normalized RDH, ESP, and WLE over $D_u \times D_v$ collecting discretizing values into 10^4 bins (Figure 4 B-D). Pairwise comparisons of normalized DPC, RDH, ESP, and WLE arrays were evaluated using Pearson correlation coefficients (PCC) and mean squared errors (MSE). Results are visualized in heatmaps (Figure 4 E).

The PCC and MSE matrices show a tightly integrated relationship between DCP and other complexity measures such as RDH and WLE, highlighted by exceptionally high correlations (DCP-RDH: 0.965, DCP-WLE: 0.959) and very low MSE values (DCP-RDH: 0.0028, DCP-WLE: 0.0034), suggesting that these measures evaluate closely related dimensions of image complexity, particularly in structural and textural aspects. In contrast, ESP exhibits lower correlations with DCP (0.265) and correspondingly higher MSE values, indicating that it captures a distinct dimension of complexity that diverges from the properties assessed by DCP, RDH, and WLE. This pattern underscores ESP's unique contribution to complexity analysis, providing insights that extend beyond those derived from conventional structural and textural metrics, thereby enriching the comprehensive understanding of image complexities.

We further plot all normalized DPC and DNOS values for all D_u, D_v pairs in the plane (Figure 3G) with same method as described in (Section 2.3). Rather than showing a distinct separation into clusters as in (Figure 4F), a more complicated picture emerges where clusters form regions spread over the whole D_u, D_v plane. This suggests that some sets of parameters allow the PDE system to evolve pattern with higher complexity and diversity than others.

To better understand which parameter values of D_u, D_v that underlie the clusters (Figure 4G) we relate the clusters to the contour plots of normalized DPC and DNOS (Figure 4H). As it was the case for the linear Turing model (Figure 3G) we find that the cluster regions

separate the parameter space of D_u and D_v into distinct regions (indicated by the diagonal bands), indicating that some parameter values of D_u, D_v form higher pattern complexity and pattern diversity.

For each cluster around the centroids we select 20 representative samples (see section 2.3) for a more detailed description of the procedure involved) and display these in a grid format, organized by cluster and sorted by complexity, to provide insights into the system's dynamic patterns (Figure 4I).

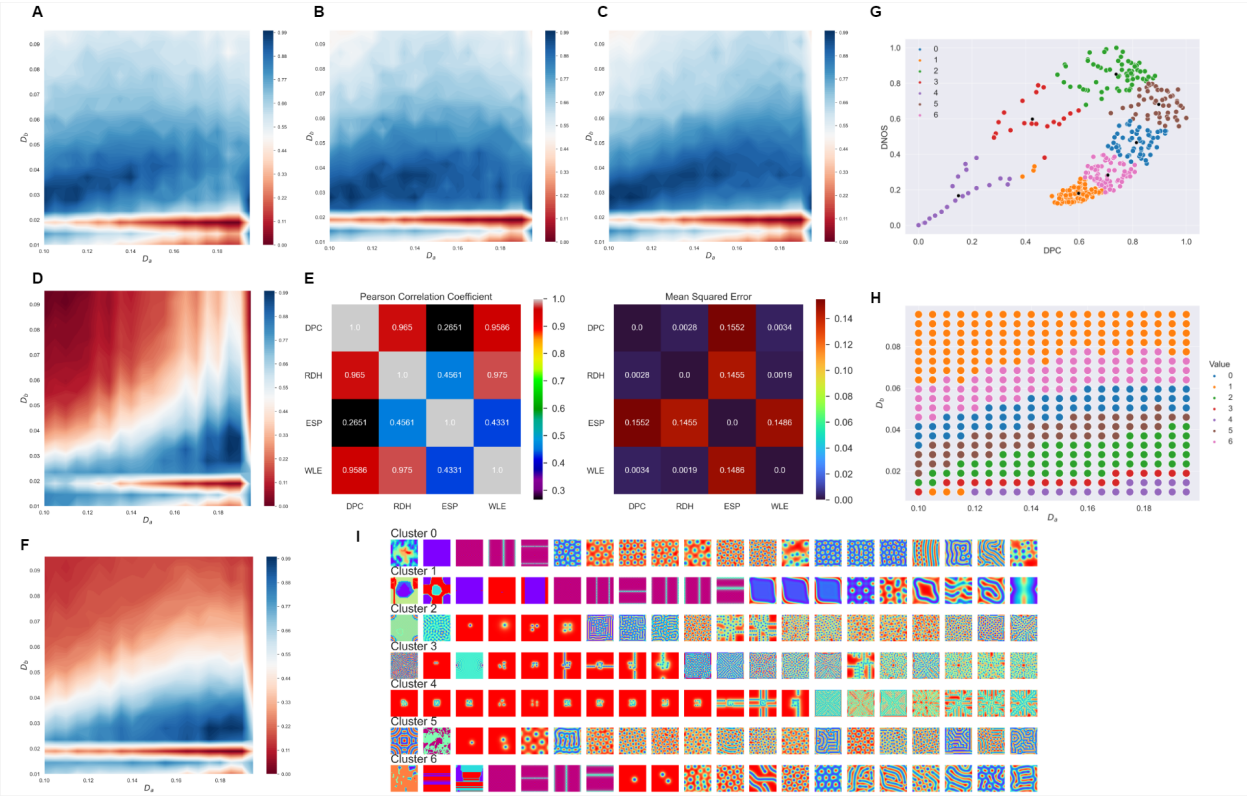

Figure 4: The Gray-Scott model: **A-D:** Showing contour plot of normalized DCP, and other pattern complexity measures over $D_u \times D_v$ using discretizing values into 10^4 bins. **A:** DCP **B:** Discretizing wavelet energy ratio (WLE). The wavelet energy ratio is calculated by applying a two-dimensional discrete wavelet transform to decompose the image into approximation and detail components. The energy ratio, reflecting the complexity and texture, is the ratio of the detail energy to the approximation energy. **C:** Resistance Distance Histogram (RDH). The RDH is derived from a graph based on image concentrations, with resistance distances computed from the graph Laplacian matrix. **D:** Discretizing spectral energy based on discrete Fourier transform (ESP). Spectral energy is calculated using a Fourier transform, with energy determined by summing the squared magnitude spectrum values, indicating frequency content and complexity. **E:** Pairwise comparisons of normalized DPC, RDH, ESP, and WLE arrays were evaluated using Pearson correlation coefficients and mean squared errors (MSE). Results are visualized in correlation and MSE heatmaps. **F:** Showing a contour plot of normalized DNOS values over $D_u \times D_v$. **G:** Showing a scatter plot of normalized DPC and DNOS values for all D_u and D_v pairs in a plane DPC over $DNOS$. Data points were clustered via KMeans. **H:** Mapping the clusters from **G** onto all D_u and D_v pairs in the plane DPC over $DNOS$., **I:** KMeans clustering was employed to identify representative data points. Images were generated from binned data, 20 representative samples were selected, sorted by complexity, and displayed in a grid organized by cluster.

2.5 The FitzHugh-Nagumo model

The FitzHugh-Nagumo (FHN) model is a simplified version of the Hodgkin-Huxley model Hodgkin and Huxley [1952], developed to describe the excitable dynamics of neurons with less computational complexity. Originally formulated by Richard FitzHugh FitzHugh [1961] in the early 1960s and further refined by Jinichi Nagumo Jinichi Nagumo and Yoshizawa [1962], this model captures key neuronal behaviors, such as excitability and oscillations, through a system of nonlinear differential equations. The basic form of the FHN model consists of two coupled equations that represent the membrane voltage of a neuron and the recovery variable, which corresponds to the inactivation of sodium channels and the activation of potassium channels. The FHN model's simplicity and robustness have led to its widespread use in various fields beyond neuroscience, including cardiology, where it helps simulate cardiac dynamics and spiral wave patterns, and chemistry, where it models reaction-diffusion systems and chemical turbulence Daniel Cebrian-Lacasa and Gelens [2024].

The model is particularly valuable in studying pattern formation due to its ability to generate a wide range of spatiotemporal patterns, such as traveling waves and Turing patterns. These patterns emerge from the interaction between reaction kinetics and diffusion processes, governed by linear stability analysis and bifurcation theory Daniel Cebrian-Lacasa and Gelens [2024]. In biological contexts, the FHN model has been used to investigate the propagation of action potentials in neuronal networks and cardiac tissues, providing insights into synchronization and the emergence of complex dynamics Daniel Cebrian-Lacasa and Gelens [2024]. However, challenges remain, particularly in accurately capturing the intricate dynamics of real biological systems and extending the model to higher-dimensional problems, which require sophisticated numerical methods and stability analyses Daniel Cebrian-Lacasa and Gelens [2024].

The inclusion of diffusion terms allows the FHN model to simulate Turing patterns, which are crucial for understanding complex spatial patterns in biological and chemical systems. The model provides a robust framework for studying the interplay between reaction kinetics and diffusion, facilitating the emergence of intricate patterns characteristic of Turing systems. This computational adaptation is essential for simulating and elucidating pattern formation in various biological contexts Daniel Cebrian-Lacasa and Gelens [2024].

In our analysis we are using an adaption of the FitzHugh-Nagumo model as a 2D reaction-diffusion system Gambino et al. [2018], which describes a similar process of pattern formation through the dynamics of an activator (a) and an inhibitor (b):

$$\frac{\partial a}{\partial t} = D_a \nabla^2 a + f(a,b), \tag{7}$$

$$\frac{\partial b}{\partial t} = D_b \nabla^2 b + g(a,b), \tag{8}$$

$$f(a,b) = a - a^3 - b + \alpha, \tag{9}$$

$$g(a,b) = \beta(a - b), \tag{10}$$

In this system, a and b denote the activator and inhibitor, respectively, with diffusion coefficients D_a and D_b. The interaction terms $a - a^3 - b + \alpha$ and $\beta(a - b)$ define the reaction kinetics, modulated by parameters α and β. The term $a - a^3$ captures the cubic

nonlinearity typical of excitable systems, representing the activator's self-regulation, while $-b$ and $\beta(a-b)$ represent the inhibitory effects and the coupling between the activator and inhibitor, respectively.

Using the same setup as in (Section 2.4) we collect outputs after 10^2 time steps for all combinations of diffusion coefficients D_u and D_v and the parameters a and b. A complete set of parameters used and their respective ranges are shown in (Table 3).

Parameter	**Description**	**Range**	**Increment**
D_u	Diffusion rate of u	1 to 50	2.5
D_v	Diffusion rate of v	1 to 100	5
a	Reaction rate for u	0 to 0.1	0.005
b	Interaction of v with u	0 to 0.1	0.005
dx	Spatial resolution	1	
dt	Time step	0.001	

Table 3: Summary of the parameters and their ranges explored in the simulation.

We show contour plots of normalized DPC and DNOS values over the D_u, D_v plane respectively collecting discretizing values into 10^4 bins (Figure 5 A,F). Again, we create contour plots of the additional measures of pattern complexity RDH, ESP and WLE with DCP (Figure 5 B-D) and create a pairwise comparisons of normalized DPC, RDH, ESP, and WLE arrays were evaluated using PCC and MSE. Results are visualized in heatmaps (Figure 5 E).

The PCC and MSE matrices DCP exhibits extremely high correlations with RDH (0.994) and WLE (0.998), with corresponding low MSE values (DCP-RDH: 0.00166, DCP-WLE: 0.00029), indicating that these measures assess highly similar dimensions of image complexity. The near-perfect alignment in their outputs suggests that changes in decomposition pattern complexity (DCP) are almost identically reflected in the measures of topological complexity (RDH) and wavelet energy ratio (WLE). In contrast, ESP shows weak negative correlations with DCP and higher MSE values (DCP-ESP: 0.20002). These findings are very similar as in (Section 2.4)

Following the same procdeure as in (Section 2.4) we plot all normalized DPC and DNOS values for all D_u, D_v pairs in the plane. Figure 5G) shows a separation into regions (we call these clusters as identified via k-means clustering). In contrast to (Figure 5G) the data points are organized into distinct bands of increasing DNOS values. Notably, cluster 2 (green) occupies the upper right quadrant of the plane suggesting that some sets of parameters allow the PDE system to evolve pattern with higher complexity and diversity than all the other parameter combinations explored.

Again, we relate the clusters (Figure 5G) to the contour plots of normalized DPC and DNOS (Figure 5H). We find that the cluster regions separate the parameter space of D_u and D_v into distinct regions (indicated by the distinct rectangular shaped regions), indicating again that some parameter values of D_u, D_v form higher pattern complexity and pattern diversity.

Following same procedure as in (Section 2.4) we select 20 representative samples for each cluster around the centroids and display these in a grid format, organized by cluster and sorted by complexity, to provide insights into the system's dynamic patterns (Figure 5I).

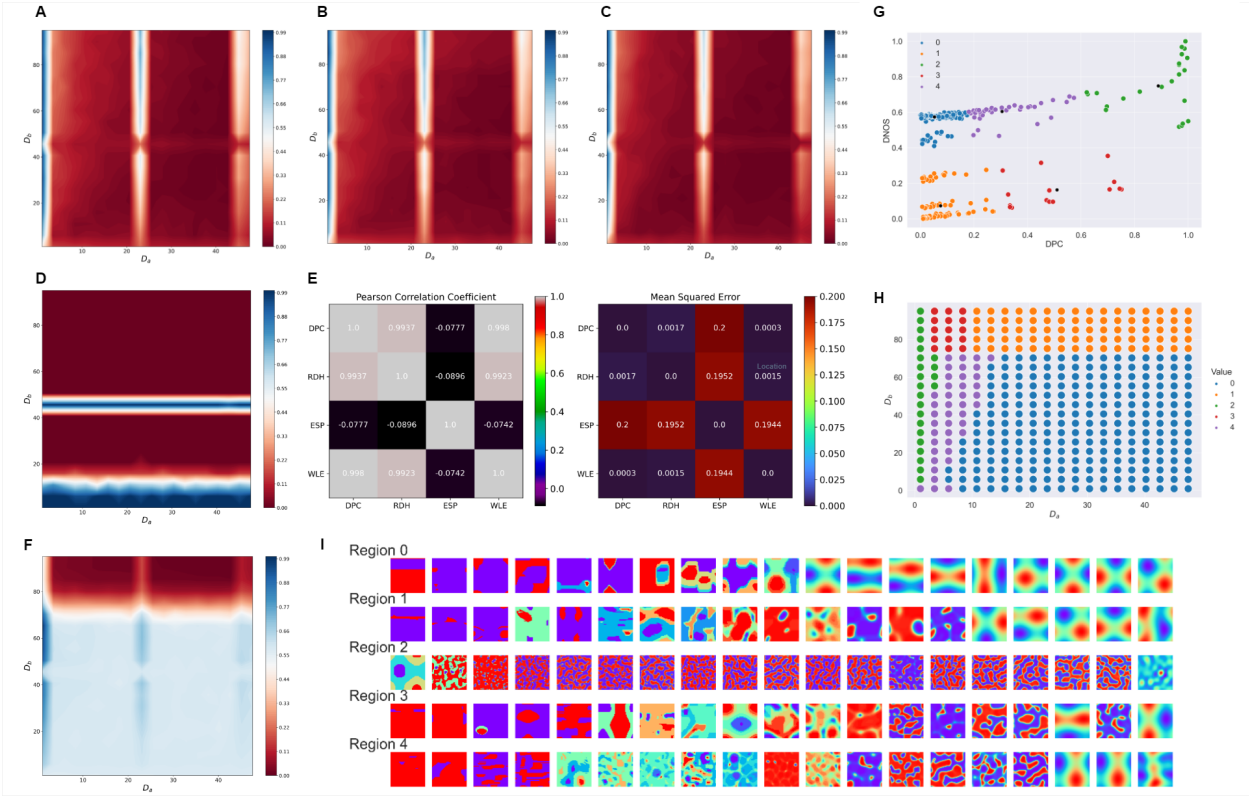

Figure 5: The FitzHugh-Nagumo model: **A-D:** Showing contour plot of normalized DCP, and other pattern complexity measures over $D_u \times D_v$ using discretizing values into 10^4 bins. **A:** DCP **B:** Discretizing wavelet energy ratio (WLE). **C:** Resistance Distance Histogram (RDH). **D:** Discretizing spectral energy (ESP). **E:** Pairwise comparisons of normalized DPC, RDH, ESP, and WLE arrays were evaluated using Pearson correlation coefficients and mean squared errors (MSE). Results are visualized in correlation and MSE heatmaps. **F:** Showing a contour plot of normalized DNOS values over $D_u \times D_v$. **G:** Showing a scatter plot of normalized DPC and DNOS values for all D_u and D_v pairs. Data points were clustered via KMeans. **H:** Mapping the clusters from **G** onto all D_u and D_v., **I:** KMeans clustering was employed to identify representative data points. Images were generated from binned data, 20 representative samples were selected, sorted by complexity, and displayed in a grid organized by cluster.

2.6 Spatiotemporal patterning enabled by gene regulatory networks

Gene regulatory networks (GRNs) are fundamental to spatiotemporal pattern formation in biological systems, orchestrating the precise regulation of gene expression necessary for processes such as tissue development and cell differentiation MacArthur et al. [2009], Paulsson [2004]. Central to these networks is the toggle switch, a bistable regulatory motif composed of two mutually repressing genes, which enables cells to commit to distinct fates and maintain stable expression states Roeder and Glauche [2006], Cherry and Adler [2000]. The toggle switch, a key gene regulatory motif, governs binary cell fate decisions in mammalian development by ensuring stable lineage commitment through mutual inhibition of opposing transcription factors ZHO [2011]. Notably, the GATA1-PU.1 switch controls erythroid and myeloid differentiation, highlighting the toggle switch's role in maintaining stable states critical for irreversible cell differentiation within the hierarchical tree of cell fates. When coupled with 2D diffusion, where signaling molecules or morphogens spatially propagate through tissues, the toggle switch can drive the formation of spatially distinct gene expression patterns Perez-Carrasco et al. [2016], Warren and ten Wolde [2004]. This interplay between bistability and spatial diffusion is crucial for establishing sharp boundaries and organized cellular structures in developing tissues Kepler and Elston [2001]. Moreover, introducing self-activation, where one or both genes in the toggle switch positively regulate their own expression, adds complexity by potentially generating tristability or multi-attractor dynamics, further enhancing the robustness and intricacy of the patterns formed Chickarmane et al. [2006], Strasser et al. [2011]. Studying toggle switches with 2D diffusion, both with and without self-activation, is critical for understanding the mechanisms by which GRNs enable spatiotemporal patterning, offering insights into key developmental processes and the potential consequences of dysregulation in diseases such as cancer Huang et al. [2009].

In the following sections we study two models, Toggle Switch with 2D Diffusion and Toggle Switch with 2D Diffusion and Self-Activation as described in Roy et al. [2023]. The toggle switch, a bistable motif, coupled with 2D diffusion, allows for the exploration of how local gene expression differences propagate spatially, generating stable patterns. Adding self-activation introduces a third stable state (tristability), reflecting more complex dynamics seen in biological processes, such as cell lineage decisions, and enhances the robustness and diversity of emergent patterns.

2.6.1 Toggle switch with 2D diffusion

The toggle switch model consists of two genes, A and B, that mutually inhibit each other. The model is extended to include diffusion, essential for spatial pattern formation. The dynamical system is described by the following equations:

The time evolution of the concentrations of proteins A and B due to regulatory interactions and diffusion is given by the partial differential equations:

$$\frac{\partial [A]}{\partial t} = D_A \nabla^2 [A] + g_A \cdot H_{B \to A} - \gamma_A \cdot [A], \tag{11}$$

$$\frac{\partial [B]}{\partial t} = D_B \nabla^2 [B] + g_B \cdot H_{A \to B} - \gamma_B \cdot [B], \tag{12}$$

with protein concentrations $[A]$, $[B]$, diffusion coefficients $D_{A,B}$, transcription rates $g_{A,B}$, degradation rates $\gamma_{A,B}$, and spatial diffusion via ∇^2. The interaction terms $H_{B\to A}$ and $H_{A\to B}$ are Hill functions $\frac{X_0^n}{X^n+X_0^n} + l \cdot \frac{X^n}{X^n+X_0^n}$ for inhibition, with X as inhibitor concentration, X_0 threshold, l fold-change, and n Hill coefficient.

We numerically solve the PDE system using the finite-difference method (Section 4.2) and conduct a simulation on a 2D grid with dimensions of 5.0 mm x 5.0 mm, discretized into 50 x 50 points with a grid spacing of 0.1 mm in both the x- and y-directions, resulting in grid point spacings of 0.01 mm^2. The initial values for the matrices u and v are set to 100. The diffusion coefficient D is set at 0.001. Time integration is performed with a time step size (dt) of 0.1 for a total of 500 steps. Hill function parameters include fold changes ($\lambda_{A\to B}$ and $\lambda_{B\to A}$) both set at 0.1, degradation rates (γ) randomly chosen between 0 and 1, and production rates (g) ranging from 1 to 50. The exponents for Hill functions ($n_{A\to B}$ and $n_{B\to A}$) vary from 1 to 6 in increments of 0.25, and threshold values (A_{0B} and B_{0A}) range from 1 to 10 in increments of 1. A parameter grid is created by iterating over these ranges, generating 10 random sets of gamma and g values for each combination of $n_{A\to B}$, $n_{B\to A}$, A_{0B}, and B_{0A}.

We show contour plots of normalized DPC (Figure 6 A) and DNOS (Figure 6 B) values over the Hill function exponents $n_{A\to B}$, $n_{B\to A}$ vary from 1 to 6 in increments of 0.25, and threshold values (A_{0B} and B_{0A}) range from plane respectively collecting discretizing values into 10^4 bins. The pattern complexity (DPC) depends on the parameter values of $n_{A\to B}$ and $n_{B\to A}$ as shown in more or less diagonal regions (blue) indicating a regimes where pattern formation is favoured alternating with bands (red) where pattern formation is less favourable. In contrast, DNOS values seam to be low for all parameter values of $n_{A\to B}$ and $n_{B\to A}$. No discernable pattern emerges.

In (Figure 6 C) we show a scatter plot of normalized DPC and DNOS values, clusters are identified via KMeans clustering, showing distinct groupings within the DPC/DNOS space. Most of the data points lie in the region with low DNOS values (below 0.2) but exhibit a wide range of DPC values. Clusters 0, 1, 2, and 6 occupy this lower DNOS regime, reflecting patterns with minimal state diversity but varying levels of pattern complexity. Cluster 5 has more scattered DNOS values, suggesting greater state diversity with moderate DPC values. Clusters 4 and 3 exhibit higher DNOS values, indicating a richer state diversity, with Cluster 4 reaching both high DNOS and DPC, corresponding to the most complex pattern formations. This distribution highlights that while pattern complexity (DPC) can vary significantly, the majority of patterns maintain low state diversity (DNOS), suggesting constrained variability in system states even as pattern complexity increases across certain regimes.

2.6.2 Toggle switch with 2D diffusion and self-activation

This model extends the basic toggle switch by incorporating self-activation loops for each gene, resulting in a more complex gene regulatory network. The system is described by a set of partial differential equations that account for both gene regulatory interactions and spatial diffusion.

The time evolution of the concentrations of proteins A and B, accounting for mutual inhibition and self-activation, is given by the partial differential equations:

$$\frac{\partial[A]}{\partial t} = D_A \nabla^2[A] + g_A \cdot H_{A\to A} \cdot H_{B\to A} - \gamma_A \cdot [A], \tag{13}$$

$$\frac{\partial[B]}{\partial t} = D_B \nabla^2[B] + g_B \cdot H_{B\to B} \cdot H_{A\to B} - \gamma_B \cdot [B], \tag{14}$$

with $[A]$, $[B]$ as protein concentrations, $g_{A,B}$ transcription rates, $\gamma_{A,B}$ degradation rates, $D_{A,B}$ diffusion coefficients, and ∇^2 for spatial diffusion. The Hill functions $H_{A\to A}$, $H_{B\to B}$, $H_{B\to A}$, $H_{A\to B}$ denote self-activation and mutual inhibition interactions, defined as $H(X, X_0, l, n) = \frac{X_0^n}{X^n+X_0^n} + l \cdot \frac{X^n}{X^n+X_0^n}$ for effector concentration X, threshold X_0, fold-change l, and Hill coefficient n.

We investigate the spatial-temporal dynamics of a toggle switch gene regulatory network with self-activation and diffusion on a two-dimensional (2D) grid. The grid measures 2.0 mm by 2.0 mm, discretized into 20 x 20 points with a grid spacing of 0.1 mm. Initial gene concentration matrices u and v are set to 100, with a diffusion coefficient of 0.00001. Time integration is performed with a step size of 0.1 over 5000 steps.

Key parameters include Hill function fold changes ($\lambda_{A\to A} = 3.0$ and $\lambda_{A\to B} = 0.1$). Degradation rates (γ) range from 0 to 1, and production rates (g) range from 1 to 50. Hill function exponents ($n_{A\to A}$ and $n_{A\to B}$) vary from 1 to 6 in increments of 0.2, while threshold values (A_{0A} and A_{0B}) range from 1 to 6 in increments of 0.25. A parameter grid is generated by iterating over these ranges, producing 1 random set of gamma and g values for each combination.

We show contour plots of normalized DPC (Figure 6 E) and DNOS (Figure 6 F) values over the Hill function exponents $n_{A\to B}$, $n_{B\to A}$ vary from 1 to 6 in increments of 0.25, and threshold values (A_{0B} and B_{0A}) range from plane respectively collecting discretizing values into 10^4 bins. The pattern complexity (DPC) depends on the parameter values of $n_{A\to B}$ and $n_{B\to A}$ as shown in diagonal regions (blue) indicating a regimes where pattern formation is favoured alternating with bands (red) where pattern formation is less favourable. In comparison to the 2D Diffusion without self-activation case the separation of high pattern diversity (high DCP values) and low pattern diversity (low DCP values) is much more defined. The 2D Diffusion without self-activation did not show any diverity in the DNOS values, in the case with self-activation, DNOS values follow a similar separation of regions of high DNOS values and low DNOS values for all parameter values of $n_{A\to B}$ and $n_{B\to A}$ (shown as diagonal red and blue) stripes).

The scatter plot of normalized DPC and DNOS values (Figure 6 G) shows a positive correlation between pattern complexity and state diversity, with six distinct clusters identified via KMeans. Clusters with low DPC and DNOS (e.g., Cluster 1) indicate simple patterns with minimal state diversity, while those with high values (e.g., Cluster 4) represent complex patterns and a diverse range of states. Intermediate clusters (e.g., Cluster 0) show moderate complexity and state diversity, highlighting parameter regimes where intricate patterns can emerge even with constrained state diversity. This clustering underscores the varying degrees of complexity in pattern formation across different parameter settings.

Overall, the figure (Figure 6 G) displays richer dynamics in both state and pattern complexity, while the figure (Figure 6 C) emphasizes complex pattern formation within more limited state spaces.

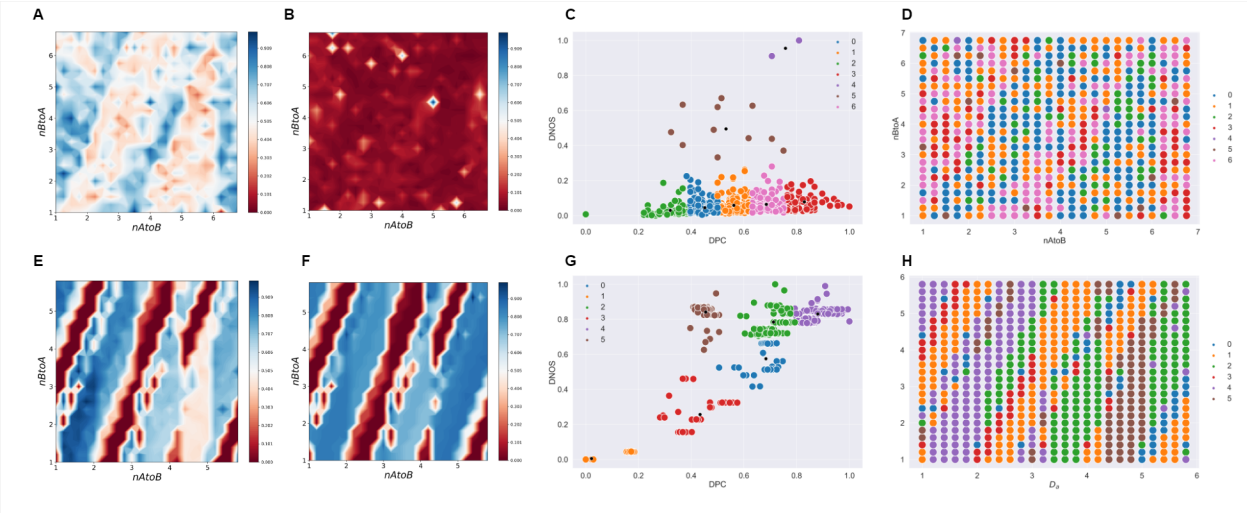

Figure 6: Toggle switch with 2D diffusion: **A:** Discretizing pattern complexity and number of states values into 10^4 bins, showing a contour plot of normalized DPC values over $D_u \times D_v$., **B:** Discretizing number of states values into 10^4 bins, showing a contour plot of normalized DNOS values over $D_u \times D_v$., **C:** Using Uniformity Measure of Entropy and discretizing pattern complexity and number of states values into 10^4 bins, showing a scatter plot of normalized DPC and DNOS values for all D_u and D_v pairs in a plane DPC over $DNOS$. Data points were clustered. **D:** Showing a scatter plot mapping the clusters from **G** (discretizing pattern complexity and number of states values into 10^4 bins) onto all D_u and D_v pairs in the plane DPC over $DNOS$., Toggle switch with 2D diffusion and sel-activation: **E:** Discretizing pattern complexity and number of states values into 10^4 bins, showing a contour plot of normalized DPC values over $D_u \times D_v$., **F:** Discretizing number of states values into 10^4 bins, showing a contour plot of normalized DNOS values over $D_u \times D_v$., **G:** Discretizing pattern complexity and number of states values into 10^4 bins, showing a scatter plot of normalized DPC and DNOS values for all D_u and D_v pairs in a plane DPC over $DNOS$. Data points were clustered. **H:** Showing a scatter plot mapping the clusters from **H** (discretizing pattern complexity and number of states values into 10^4 bins) onto all D_u and D_v pairs in the plane DPC over $DNOS$.

2.7 The DNOS and DPC compute space

This section analyzes the Uniformity Measure of Entropy (UME) for both compression ratios (UME(CR)) and state values (UME(S)) across five gene regulatory network models: Linear Turing (LINTP) (Section 2.3), Gray-Scott (GSM) (Section 2.4), FitzHugh-Nagumo (FHN) (Section 2.5), toggle switch with 2D diffusion (TGLS) (Section 2.6.1), and toggle switch with 2D diffusion and self-activation (TGLSWA) (Section 2.6.2). In Figure 7, GSM, FHN, and TGLSWA occupy the upper-right quadrant, with UME(CR) values around 0.85 and UME(S) ranging from 0.5 to 1.0. This indicates a high degree of uniformity in both state distributions and pattern complexity, particularly for GSM, which shows near-perfect uniformity in state distribution with a UME(S) of 1.0. FHN and TGLSWA exhibit slightly lower UME(S) values (0.6 and 0.5, respectively), reflecting high complexity uniformity but with more heterogeneous state distributions. LINTP, located in the lower-right quadrant, exhibits the highest UME(CR) (1.0) but moderate UME(S) (0.45), suggesting uniform complexity but a more uneven distribution of state values, indicating greater variability in state diversity. TGLS, positioned in the lower-left quadrant, shows low UME(CR) and UME(S) values (both near 0), reflecting minimal uniformity in both metrics, characteristic of simpler systems with low diversity. This highlights the distinctions between the models: GSM, FHN, and TGLSWA demonstrate the most uniform behavior in both metrics, while LINTP shows high complexity uniformity but more variability in state distributions, and TGLS exhibits the least uniformity across both measures.

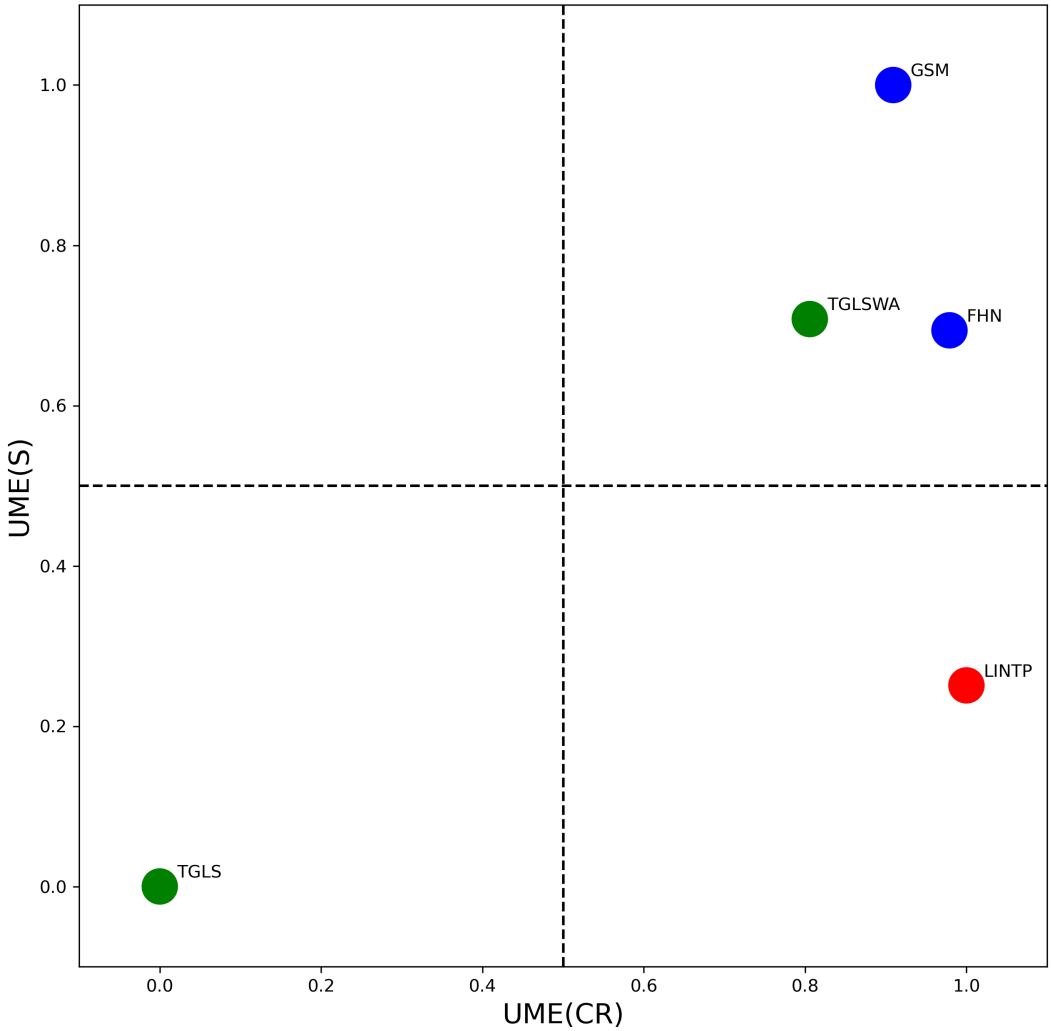

Figure 7: The Uniformity Measure of Entropy (UME) for compression ratios (UME(CR)) and state values (UME(S)) across five gene regulatory network models: Linear Turing (LINTP), Gray-Scott (GSM), FitzHugh-Nagumo (FHN), toggle switch with 2D diffusion (TGLS), and toggle switch with 2D diffusion and self-activation (TGLSWA). GSM, FHN, and TGLSWA occupy the upper-right quadrant, indicating high uniformity in both pattern complexity and state distributions, particularly for GSM (UME(S) 1.0). LINTP, in the lower-right quadrant, shows high uniformity in complexity (UME(CR) 1.0) but more variability in state distributions (UME(S) 0.45). TGLS, in the lower-left quadrant, exhibits minimal uniformity in both metrics, characteristic of simpler systems with low diversity.

2.8 Notch (N), Delta (D), and EGF (E) Signaling in Drosophila Neurogenesis

Neurogenesis in Drosophila melanogaster provides a key model for understanding nervous system development, where neural precursors differentiate into neurons and glial cells under the regulation of molecular signaling pathways, including Notch and Epidermal Growth Factor (EGF) signaling. While Notch-mediated lateral inhibition typically results in a 'salt and pepper' pattern during cell fate determination, the development of the Drosophila visual center introduces a unique 'proneural wave,' where neuroepithelial cells sequentially differentiate into neuroblasts through the expression of proneural transcription factors, such as Lethal of scute (L'sc). Unlike traditional Notch signaling, the proneural wave does not exhibit a 'salt and pepper' pattern due to the diffusion of EGF, which modulates the propagation of Notch signaling, thereby facilitating the wave's progression. Mathematical models and genetic analysis have demonstrated that the combination of EGF-mediated reaction diffusion and Notch-mediated lateral inhibition is critical for regulating this wave of differentiation, highlighting the complex interplay between signaling pathways in neurogenesis Sato et al. [2016].

Notch signaling, typically associated with binary cell fate decisions and salt-and-pepper pattern formation, exhibits a distinct behavior during the proneural wave in the Drosophila medulla, where differentiation occurs without such patterning. Unlike its role in other developmental processes, Notch signaling in this context is modulated by EGF-mediated reaction diffusion, which controls the speed of the proneural wave rather than directly influencing binary cell fate decisions. This modulation of Notch activity by EGF diffusion highlights the unique interplay between these signaling pathways in regulating neurogenesis, underscoring the complexity of Notch's function beyond its classical lateral inhibition role Sato et al. [2016].

We study in the following section in detail pattern formation in a model presented in Sato et al. [2016]. The model consists of four primary entities represented by their concentration grids: E, N, D, and A. These entities interact through diffusion and reaction processes, governed by a set of parameters. The PDEs describing the dynamics of each entity are as follows:

$$\frac{\partial E}{\partial t} = d_e \nabla^2 E - k_e E + e_e E + n_e N + a_e A(A_0 - A) + \theta_E, \tag{15}$$

$$\frac{\partial N}{\partial t} = -k_n N + dt \sum (D_{\text{neigh}}) - d_c D + \theta_N, \tag{16}$$

$$\frac{\partial D}{\partial t} = -k_d D + e_d E + a_d A(A_0 - A) + \theta_D, \tag{17}$$

$$\frac{\partial A}{\partial t} = e_a (A_0 - A) \max(E - N, 0) + \theta_A, \tag{18}$$

where ∇^2 represents the Laplacian operator. Parameters include spatial/temporal steps dx/dt, reference concentration A_0, decay rates $k_{e,n,d}$, diffusion coefficient d_e, interaction coefficients $e_{e,d,a}$, n_e, $a_{e,d}$, and stochastic terms $\theta_{E,N,D,A}$ indicating noise.

The exclusion of self-regulation and cross-regulation terms from the respective mutant cell types allows for an in-depth study of the component's role in the gene regulatory network.

Parameters ee, ae, ne, dt, and ad were set to zero based on the mutant clone being simulated. This effectively "knocks out" the pathway, providing a clearer understanding of how such mutations impact cellular behavior and development.

This study examines the dynamic pattern complexity (DPC) and the number of states (DNOS) within various gene regulatory network models, focusing on the intricate signaling pathways involved in *Drosophila* neurogenesis. The models analyzed include the wild type, Delta (Dl) mutant, EGF mutant, and Notch mutant configurations.

We numerically solve the PDE system using the finite-difference method (Section 4.2) and and conduct simulations for three distinct parameter sets, A, B, and C. The simulations operate on a 20x20 spatial grid, performing 2000 iterations for each of the 1000 parameter samples specified. Both the DPC and DNOS are calculated using 1000 bins. Table 5 details the parameter settings for the proneural wave experiments across these sets. The parameter d_e ranges from [0.0, 1.0] for sets A and B and is fixed at 1.0 for set C. Similarly, parameters such as e_d, A_0, and a_d follow the same pattern. Other parameters, including n_e, k_n, and e_a, have distinct ranges and fixed values across the different sets.

Data from three distinct simulation setups, corresponding to different parameter sets, are aggregated. This data includes outputs from wild-type and mutant simulations. The data is preprocessed to ensure consistency, including standardizing column names and labeling each model and parameter set type. The aggregated data is grouped by model type, and the mean values of DPC and DNOS are computed. These aggregated metrics are normalized using Min-Max normalization, scaling the values between 0 and 1. This normalization ensures that the data points are within a comparable range, facilitating meaningful comparisons across different models and parameter sets.

Mutations for EGF, Notch, and Dl clones were simulated by setting specific regulatory parameters to zero, as follows:

Table 4: Parameters Set to Zero in Mutant Clones

Clone Type	**Parameters Set to Zero**
EGF	ee (EGF self-regulation), ae (regulation of EGF by AS-C)
Notch	ne (Notch regulation of EGF), dt (trans-activation of Notch by Dl)
Dl	ed (Dl regulation by EGF), ad (Dl regulation by AS-C)

The normalized DPC and DNOS values are visualized in a scatter plot (Figure 8). Each point represents a model configuration, color-coded and marked according to its type and parameter set. Different colors and marker shapes are used to differentiate between the wild-type and mutant models across various parameter sets. For instance, wild-type models for parameter sets A, B, and C are represented in shades of red, while Notch, Delta, and EGF mutants are represented in shades of green, blue, and orange, respectively. The plot axes are normalized to a range of 0 to 1, with tick marks at intervals of 0.1, ensuring uniformity and clarity in the visualization. Vertical and horizontal dashed lines at the midpoint (0.5) of the axes divide the plot into quadrants, aiding in the analysis by highlighting how different models perform relative to each other in terms of complexity and state diversity.

Table 5: Combined Parameter Settings for Proneural Wave Experiments

Parameter	**Set A**	**Set B**	**Set C**
d_e	[0.0, 1.0]	[0.0, 1.0]	Fixed at 1.0
e_d	[0.0, 1.0]	[0.0, 1.0]	Fixed at 1.0
A_0	[0.0, 1.0]	[0.0, 1.0]	Fixed at 1.0
n_e	[0.0, 1.0]	[0.0, 1.0]	[0.0, 2.0]
a_d	[0.0, 1.0]	[0.0, 1.0]	Fixed at 1.0
k_n	[0.0, 1.0]	[0.0, 1.0]	Fixed at 1.0
k_e	[0.0, 1.0]	[0.0, 1.0]	Fixed at 1.0
k_d	[0.0, 1.0]	[0.0, 1.0]	Fixed at 1.0
e_e	[0.0, 1.0]	[0.0, 1.0]	[0.0, 0.4]
a_e	[0.0, 1.0]	[0.0, 1.0]	[0.0, 2.0]
e_a	[0.0, 10.0]	[0.0, 10.0]	Fixed at 10.0
d_t	Fixed at 0.01	[0.0, 1.0]	[0.0, 0.5]
d_c	Fixed at 0.25	[0.0, 1.0]	[0.0, 0.5]

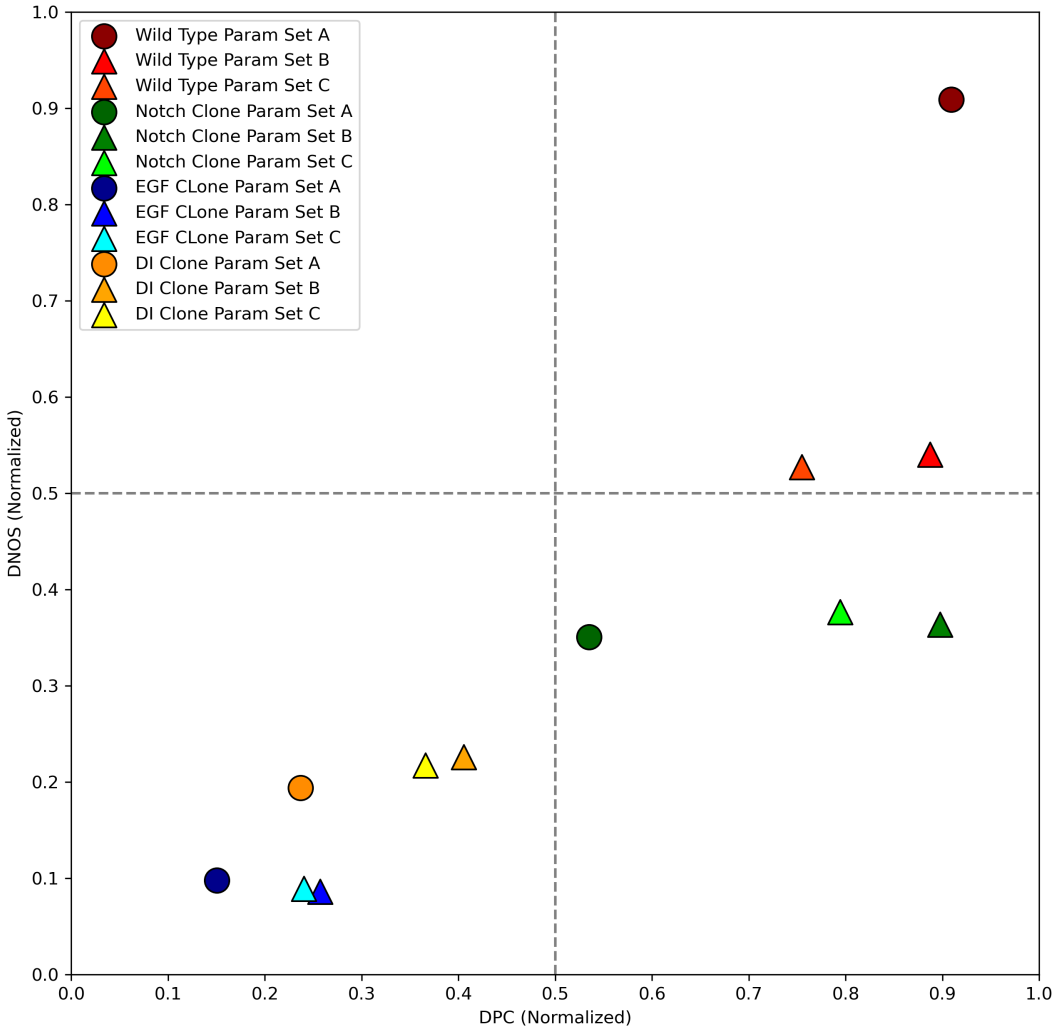

Figure 8: DPC and DNOS across gene regulatory network models in Drosophila neurogenesis. Models include wild type, Delta (Dl) mutant, EGF mutant, and Notch mutant. Data from three simulation parameter sets (A, B, C) were aggregated and normalized using Min-Max scaling (0–1). Simulations were conducted on a 20×20 spatial grid over 2000 iterations with 1000 parameter samples each. The scatter plot illustrates normalized DPC versus DNOS, with points color-coded by model type—wild type in red, Notch mutants in green, Dl mutants in blue, and EGF mutants in orange—and shaped according to parameter set. Dashed lines at 0.5 on both axes divide the plot into quadrants, highlighting differences in pattern complexity and state diversity among models and parameter configurations.

3 Discussion

Our study introduces two novel complexity measures—the Diversity of Number of States (DNOS) and the Diversity of Pattern Complexity (DPC)—to quantitatively analyze and classify patterns formed in reaction-diffusion systems, specifically focusing on Turing pat-

terns. Traditional analytical methods, particularly linear stability analysis, while effective in identifying conditions for pattern onset, are limited in predicting the long-term behavior and complexity of emergent patterns due to their linear approximations and neglect of nonlinear dynamics. This limitation hinders a comprehensive understanding of the multifaceted patterns that can arise, including bistable and multistable state distributions critical in biological contexts.

Our complexity measures address these limitations by capturing both the diversity of states and the intricacy of patterns, enabling a more nuanced exploration of the computational potential inherent in reaction-diffusion systems. The DNOS quantifies the number of distinct states within a pattern, reflecting the system's capacity for multistability and complex state distributions. The DPC assesses the structural complexity of the patterns, particularly relevant for patterns that emerge from wave-based interactions—a primary mechanism of computation in these systems [A and BDL, 2012].

In the context of the linear Turing model, our analysis shows distinct clusters in the DNOS-DPC space, correlating with specific regions in the parameter space of diffusion coefficients D_u and D_v. These clusters indicate that certain combinations of diffusion rates lead to higher pattern diversity and complexity, which traditional linear stability analysis might not fully capture. The identification of patterns with high DPC but low DNOS suggests the system's ability to generate intricate patterns from a limited set of states, typical for the generation of Turing patterns due to differences in diffusion rates between reactants and inhibitors.

Our findings align with the known capability of reaction-diffusion systems to solve geometrical problems, such as constructing Voronoi diagrams and skeletons of planar shapes, through the propagation and interaction of chemical waves [A and BDL, 2012]. The wave-based computation inherent in these systems is reflected in the high DPC values observed in models like the Gray-Scott and FitzHugh-Nagumo systems, which produce complex patterns including self-replicating spots and oscillatory behaviors [Daniel Cebrian-Lacasa and Gelens, 2024]. The capacity to create both stationary and dissipative structures [A and BDL, 2012] is captured by our complexity measures, offering quantitative insights into the dynamic behaviors of these systems.

Our study also underscores the significance of external controls in guiding pattern formation. Reaction-diffusion systems can be programmed to achieve specific patterns and state distributions by manipulating external factors such as diffusion coefficients, reaction parameters, light, temperature, and electric fields [**?**]. This programmability is evident in the variation of DNOS and DPC across different models and parameter sets, highlighting the potential to "reprogram" these systems to create different distributions of states.

In biological systems, the ability to generate and maintain complex patterns is essential for processes like embryonic development and tissue morphogenesis. The gene regulatory network models we analyzed, particularly the toggle switch with 2D diffusion and self-activation, demonstrated higher DNOS and DPC values, reflecting increased pattern diversity and complexity due to nonlinear feedback loops. This mirrors biological mechanisms where multistability and bistability play key roles in cell fate determination and the formation of spatial patterns [Roy et al., 2023].

Our analysis of the Notch-Delta-EGF signaling pathway in *Drosophila* neurogenesis further illustrates how variations in DNOS and DPC provide insights into the effects of genetic

perturbations on pattern formation. The ability of reaction-diffusion systems to exhibit both stationary Turing patterns and dynamic dissipative structures [A and BDL, 2012] is captured by our complexity measures, offering a quantitative framework to study the dynamic behavior of such biological networks.

4 Methods

4.1 Turing Model Stability Analysis

In this section we describe a detailed stability analysis with maximum mathematical rigor and detail, considering all stability and instability regions, fixed points, and bifurcations.

The inherent nonlinear nature of the reaction functions $f(u, v)$ and $g(u, v)$ is often simplified through linearization around an equilibrium point (u_0, v_0):

$$\begin{aligned} f(u,v) &\approx f(u_0,v_0) + \frac{\partial f}{\partial u}(u_0,v_0)(u-u_0) + \frac{\partial f}{\partial v}(u_0,v_0)(v-v_0), \\ g(u,v) &\approx g(u_0,v_0) + \frac{\partial g}{\partial u}(u_0,v_0)(u-u_0) + \frac{\partial g}{\partial v}(u_0,v_0)(v-v_0). \end{aligned} \tag{19}$$

This simplifies the original nonlinear reaction-diffusion equations to a set of linear PDEs.

Applying this to our linear Turing model and if the diffusion terms are ignored, it is easy to show that this system has only one equilibrium point $(u0 = h, v0 = k)$. This equilibrium point can be stable for many parameter values for a,b,c, and d. However, introducing spatial dimensions and diffusion terms to the equations may destabilize the equilibrium, and thus the system may spontaneously self-organize into a non-homogeneous pattern. We can relate the constants a, b, c, and d to the partial derivatives of the reaction functions at the equilibrium point: $a = \frac{\partial f}{\partial u}(u_0, v_0)$, $b = \frac{\partial f}{\partial v}(u_0, v_0)$, $c = \frac{\partial g}{\partial u}(u_0, v_0)$, and $d = \frac{\partial g}{\partial v}(u_0, v_0)$.

One can now convert the PDE equations into a matrix equation describing the system is given by:

$$A = \begin{bmatrix} a & b \\ c & d \end{bmatrix} \tag{20}$$

$$\mathcal{D} = det(A) \tag{21}$$

$$\mathcal{T} = Tr(A) \tag{22}$$

$$\lambda \begin{bmatrix} \hat{u}(k) \\ \hat{v}(k) \end{bmatrix} = \begin{bmatrix} a - D_u k^2 & b \\ c & d - D_v k^2 \end{bmatrix} \begin{bmatrix} \hat{u}(k) \\ \hat{v}(k) \end{bmatrix} \tag{23}$$

One can now find the eigenvalues of the matrix A by considering the characteristic equation of the matrix:

$$\det(\mathbf{A} - \lambda \mathbf{I}) = \lambda^2 - \lambda \mathcal{T}^2 + \mathcal{D} \tag{24}$$

and by finding the solutions of the quadratic equation:

$$\lambda_{1,2} = \frac{1}{2}\left(\mathcal{T} \pm \sqrt{\mathcal{T}^2 - 4\mathcal{D}}\right) \tag{25}$$

Based on the nature of the derived eigenvalues one can infer when the system is stable against small perturbation and when it is unstable. Here are the main cases:

We consider various stability cases:

I. Stability and Instability

1. Stable Fixed Point: Both eigenvalues have negative real parts.
   - $\lambda_1 < 0$ and $\lambda_2 < 0$

2. Unstable Fixed Point: At least one eigenvalue has a positive real part.
   - $\lambda_1 > 0$ or $\lambda_2 > 0$

II. Saddle Points

1. A saddle point occurs when one eigenvalue has a positive real part, and the other has a negative real part.
   - $\lambda_1 > 0$ and $\lambda_2 < 0$

2. $\lambda_1 < 0$ and $\lambda_2 > 0$

III. Bifurcations

1. Bifurcations occur when one or both eigenvalues cross zero as a parameter varies, leading to qualitative changes in the system's behavior.

Transcritical Bifurcation: One eigenvalue passes through zero as a parameter changes.
- $\lambda_1 = 0$ or $\lambda_2 = 0$

Pitchfork Bifurcation: Both eigenvalues simultaneously pass through zero as a parameter changes.
- $\lambda_1 = \lambda_2 = 0$

IV. Hopf Bifurcation

Hopf bifurcation occurs when the eigenvalues become purely imaginary, giving rise to oscillatory behavior.
This requires the discriminant of the characteristic equation to be zero:
- $(a + d - D_u k^2 - D_v k^2)^2 - 4(ad - bc - D_u D_v k^4 + (aD_v + dD_u)k^2) = 0$

The stability and instability regions, fixed points, and bifurcations can be found by analyzing the eigenvalues and discriminant for different combinations of parameters and the wave vector k. Due to the complexity of the stability analysis, numerical methods are commonly employed to determine the stability and instability regions, fixed points, and bifurcations. By systematically varying the parameters and wave vector k, one can numerically solve the characteristic equation and compute the eigenvalues. These results can then be used to identify different stability cases and investigate the behavior of the system under specific conditions.

Given the Jacobian matrix for a Turing pattern system,

$$J = \begin{pmatrix} a - D_a k^2 & b \\ c & d - D_b k^2 \end{pmatrix}, \tag{26}$$

where a, b, c, and d are system parameters, D_a and D_b are the diffusion coefficients, and k is the wave number.

The characteristic equation, or dispersion relation, ω is given by,

$$\omega = \mathrm{Tr}(J) + \sqrt{\mathrm{Tr}(J)^2 - 4\mathrm{Det}(J)}, \tag{27}$$

which simplifies to,

$$\omega = a + d - (D_a + D_b)k^2 + \sqrt{4bc + (a - d - D_a k^2 + D_b k^2)^2}. \tag{28}$$

Differentiating ω with respect to k^2, we obtain,

$$\frac{d\omega}{dk^2} = -D_a - D_b + \frac{(-D_a + D_b)(a - d + (-D_a + D_b)k^2)}{\sqrt{4bc + (a - d + (-D_a + D_b)k^2)^2}}. \tag{29}$$

Solving $\frac{d\omega}{dk^2} = 0$ for k^2, we find,

$$k^2 = \frac{(a - d)D_a(D_a - D_b)D_b \pm \sqrt{-bcD_aD_b(D_a^2 - D_b^2)^2}}{D_a(D_a - D_b)^2 D_b}. \tag{30}$$

This solution gives the values of k^2 at which the growth rate ω reaches its extremum, indicating the scale of Turing patterns for given system parameters.

The characteristic length scale L of emergent Turing patterns is inversely related to the dominant wavenumber k_{dom}, where the growth rate $\lambda(k)$ is maximized. To determine k_{dom}, we perform the following steps:

First, maximize the growth rate by setting the derivative with respect to k^2 to zero:

$$\frac{d\lambda}{dk^2} = -(D_a + D_b) + \frac{(-D_a + D_b)(a - d - (D_a - D_b)k^2)}{\sqrt{4bc + (a - d - (D_a - D_b)k^2)^2}} = 0.$$

This quadratic equation in k^2 is solved numerically to obtain critical wavenumbers k_1^2 and k_2^2, retaining only real and positive solutions.

Next, select the dominant wavenumber as the larger of the valid solutions:

$$k_{\mathrm{dom}} = \max(k_1^2, k_2^2).$$

Finally, compute the pattern length scale using:

$$L = \frac{2\pi}{k_{\mathrm{dom}}}.$$

This relation indicates that the spatial periodicity of the Turing pattern is inversely proportional to the dominant wavenumber, providing a quantitative measure of the pattern's characteristic size.

4.1.1 DPC and DNOS

The compression ratio (CR) of a given reaction-diffusion pattern is calculated as follows:

Let the image be represented as a matrix $\mathbf{I} \in \mathbb{R}^{m \times n}$, where m and n are the dimensions of the image. The matrix is converted into a byte sequence, denoted as Bytes($\mathbf{I}$), which is then compressed using a gzip algorithm. Let Compress(Bytes($\mathbf{I}$)) represent the compressed byte sequence. The original size S_{original} and the compressed size $S_{\text{compressed}}$ are the lengths of the original and compressed byte sequences, respectively. The compression ratio is then given by:

$$\text{CR}(P) = \frac{S_{\text{compressed}}}{S_{\text{original}}}$$

A lower compression ratio indicates higher complexity due to the pattern having less redundancy.

The Discrete Pattern Complexity (DPC) is calculated by discretizing the compression ratios of multiple patterns and counting the number of unique bins they occupy. Let N be the number of patterns $\{P_1, P_2, \ldots, P_N\}$, and let $\text{CR}_i = \text{CR}(P_i)$ for each pattern i. The compression ratios are scaled to the desired precision by multiplying each CR_i by 10^p, where p is the precision parameter, yielding:

$$S_i = 10^p \times \text{CR}_i$$

Each scaled value S_i is rounded to the nearest integer:

$$R_i = \lfloor S_i + 0.5 \rfloor$$

The set of unique rounded values (bins) is then:

$$B = \{R_i \mid i = 1, 2, \ldots, N\}$$

Finally, the DPC is defined as the cardinality of the set B:

$$\text{DPC} = |B|$$

This represents the number of distinct complexity levels across the patterns, based on the chosen precision.

The Discrete Number of States (DNOS) quantifies the diversity of distinct states in a reaction-diffusion pattern. Given a concentration matrix $\mathbf{I} \in \mathbb{R}^{m \times m}$, where $m = \sqrt{y}$ and y is the total number of data points, DNOS is calculated by first normalizing $\mathbf{I}$ to obtain a matrix $\mathbf{N}$ with values in the range $[0, 1]$. This normalization is defined as:

$$\mathbf{N} = \frac{\mathbf{I} - \min(\mathbf{I})}{\max(\mathbf{I}) - \min(\mathbf{I})}$$

where $\min(\mathbf{I})$ and $\max(\mathbf{I})$ are the minimum and maximum values of the matrix $\mathbf{I}$, respectively.

The normalized values are then scaled and discretized by multiplying each element of $\mathbf{N}$ by 10^p, where p is a predefined precision parameter, and rounding to the nearest integer to form the matrix $\mathbf{S}$. Finally, DNOS is computed as the number of unique values in $\mathbf{S}$, denoted by:

$$\text{DNOS} = |\{S_{jk} \mid j, k \in \{1, 2, \ldots, m\}\}|$$

where S_{jk} are the elements of the matrix $\mathbf{S}$. This process provides a measure of the diversity of discretized states in the pattern.

4.1.2 Uniformity Measure of Entropy

The Uniformity Measure of Entropy (UME) quantifies the uniformity of a data distribution. Given a matrix $\mathbf{X} \in \mathbb{R}^{m \times n}$, each element X_{ij} is scaled by a factor 10^p, where p is a precision parameter, and rounded to the nearest integer:

$$\tilde{X}_{ij} = \lfloor 10^p \cdot X_{ij} + 0.5 \rfloor$$

where $\tilde{\mathbf{X}} \in \mathbb{Z}^{m \times n}$ represents the coarsened data. These coarsened values $\tilde{X}_{ij}$ are binned into $B = 10^p$ discrete bins. Let f_b denote the frequency (count) of values falling into the b-th bin, where $b \in \{1, 2, \ldots, B\}$, and let N represent the total number of elements in $\mathbf{X}$.

The probability for each bin is then defined as:

$$p_b = \frac{f_b}{N}$$

For bins with zero counts, p_b is set to 10^{-10} to avoid computational issues in the entropy calculation. The Shannon entropy H of the distribution is calculated as:

$$H = -\sum_{b=1}^{B} p_b \log_2(p_b)$$

The maximum entropy, $H_{\max}$, corresponding to a perfectly uniform distribution, is:

$$H_{\max} = \log_2(B)$$

Finally, the Uniformity Measure of Entropy (UME) is given by:

$$\text{UME} = \frac{H}{H_{\max}}$$

where UME $\in [0, 1]$. A UME value of 1 indicates a perfectly uniform distribution, while values closer to 0 indicate less uniformity in the distribution.

One now applies the general UME calculation to the array of compression ratios $\mathbf{CR} = \{\text{CR}_1, \text{CR}_2, \ldots, \text{CR}_N\}$, where CR_i is the compression ratio for the i-th pattern. Following the same process outlined above, we compute UME(CR) as follows:

- Scale and discretize the CR values:

$$S_{\text{CR}_i} = 10^p \times \text{CR}_i, \quad R_{\text{CR}_i} = \lfloor S_{\text{CR}_i} + 0.5 \rfloor$$

- Compute the frequencies f_b for each bin b based on the discretized CR values.
- Calculate the entropy H_{CR} for the distribution of CR values.
- Compute the maximum entropy $H_{\text{CR,max}}$.
- Finally, compute the UME for CR:

$$\text{UME(CR)} = \frac{H_{\text{CR}}}{H_{\text{CR,max}}}$$

This measure, UME(CR), reflects how uniformly the compression ratios are distributed across their complexity bins, offering a UME version of DPC.

In similar fashion, one applies the UME calculation to the state array $\mathbf{S} = \{S_1, S_2, \ldots, S_N\}$, where S_i represents the state values, e.g. concentrations corresponding to different regions of a reaction-diffusion pattern. The process is analogous to the calculation of UME(CR):

- Scale and discretize the state values:

$$S_{S_i} = 10^p \times S_i, \quad R_{S_i} = \lfloor S_{S_i} + 0.5 \rfloor$$

- Compute the frequencies f_b for each bin b based on the discretized state values.
- Calculate the entropy H_S for the distribution of state values.
- Compute the maximum entropy $H_{S,\max}$.
- Finally, compute the UME for state values:

$$\mathrm{UME}(S) = \frac{H_S}{H_{S,\max}}$$

This measure, UME(S), quantifies how uniformly the state values are distributed across their bins, providing a UME version of DNOS.

4.1.3 Spectral Energy

For an image represented by a matrix $\mathbf{I} \in \mathbb{R}^{m \times n}$, the spectral energy E_{spectral} quantifies the total energy of its frequency components, excluding the zero frequency. This is computed by first applying the two-dimensional discrete Fourier transform (DFT):

$$\mathbf{F}(u, v) = \sum_{x=0}^{m-1} \sum_{y=0}^{n-1} \mathbf{I}(x, y)\, e^{-2\pi i \left(\frac{ux}{m} + \frac{vy}{n}\right)},$$

for each spatial frequency (u, v). The zero frequency component is then excluded by setting $\mathbf{F}(0, 0) = 0$. Subsequently, the spectral energy is calculated as the sum of the squared magnitudes of the Fourier coefficients:

$$E_{\text{spectral}} = \sum_{u=0}^{m-1} \sum_{v=0}^{n-1} |\mathbf{F}(u, v)|^2,$$

where $|\mathbf{F}(u, v)|$ denotes the magnitude of the complex Fourier coefficients.

The spectral energy E_{spectral} measures the total power of the image's frequency content, emphasizing variations such as edges and textures. A higher E_{spectral} indicates greater complexity and richness in high-frequency components, corresponding to intricate patterns within the image.

4.1.4 Resistance Distance Histogram

For an image represented by a concentration matrix $\mathbf{C} \in \mathbb{R}^{n \times n}$, a graph $G(V, E)$ is constructed where each C_{ij} maps to a vertex v_{ij} in V. Edges (v_{ij}, v_{kl}) are formed between vertices within a neighborhood radius r if the associated concentration values meet the condition $(C_{ij} \geq \theta \wedge C_{kl} \geq \theta) \vee (C_{ij} < \theta \wedge C_{kl} < \theta)$, where θ is the mean concentration if not specified. Edges are weighted 1 if the condition is met, otherwise a small value ϵ is used.

Graph G may be optionally undersampled by a factor t, reducing the number of vertices and edges to simplify the computational requirements. Resistance distances in G are calculated by first constructing the weighted adjacency matrix Ω_G. The graph Laplacian $\mathbf{L}_G = \mathbf{D}_G - \Omega_G$ is then formed, where $\mathbf{D}_G$ is the degree matrix with entries equal to the sum of the edge weights for each vertex. The resistance distance matrix $\mathbf{R}$ is derived from the pseudoinverse $\mathbf{K}$ of $\mathbf{L}_G$, calculated as $R_{ij,kl} = K_{ii} + K_{ll} - 2K_{il}$.

The histogram of resistance distances is computed by binning $\mathbf{R}$ into a pre-defined number of bins within the range $[0, R_{\max}]$ and normalizing the histogram so the sum of its values equals one, assuming the sum is non-zero.

4.1.5 Wavelet Energy Ratio

Given an image matrix $\mathbf{A} \in \mathbb{R}^{x \times y}$, the wavelet energy ratio is computed using the biorthogonal wavelet 'bior1.3'. The two-dimensional discrete wavelet transform of $\mathbf{A}$ yields four sets of coefficients: approximation coefficients cA, horizontal detail coefficients cH, vertical detail coefficients cV, and diagonal detail coefficients cD. The energies of the detail and approximation components are calculated by summing the squares of their respective coefficients:

$$E_{\text{detail}} = \sum(cH^2) + \sum(cV^2) + \sum(cD^2)$$

$$E_{\text{approximation}} = \sum(cA^2)$$

If the approximation energy $E_{\text{approximation}}$ is non-zero, the wavelet energy ratio R is defined as the ratio of the detail energy to the approximation energy:

$$R = \frac{E_{\text{detail}}}{E_{\text{approximation}}}$$

If $E_{\text{approximation}} = 0$, R is set to zero. This metric quantifies the relative energy content in the detailed versus smoothed components of the image, essential for applications in image processing and analysis.

4.2 Numerical Simulation of the Turing Patterns PDE

Turing patterns emerge in reaction-diffusion systems, which are typically modeled by a set of coupled partial differential equations (PDEs). The finite-difference method is a numerical technique used to approximate solutions to these PDEs. We consider a simple linear form of Turing pattern PDEs for two interacting chemical species with concentrations $u(x, y, t)$ and $v(x, y, t)$:

$$\frac{\partial u}{\partial t} = f(u,v) + D_u \nabla^2 u,$$
$$\frac{\partial v}{\partial t} = g(u,v) + D_v \nabla^2 v,$$

where $f(u,v)$ and $g(u,v)$ are the reaction terms, and D_u and D_v are the diffusion coefficients.

We discretize the spatial domain into a grid with points (x_i, y_j), where $x_i = i\Delta x$, $y_j = j\Delta y$, and i, j are integers. The Laplacian ∇^2 in two dimensions is discretized using the central difference scheme:

$$\nabla^2 u \approx \frac{u_{i+1,j} + u_{i-1,j} + u_{i,j+1} + u_{i,j-1} - 4u_{i,j}}{\Delta x^2},$$

assuming $\Delta x = \Delta y$ for simplicity.

We discretize time into steps of size Δt. The time derivative is approximated using the forward difference:

$$\frac{\partial u}{\partial t} \approx \frac{u_{i,j}^{n+1} - u_{i,j}^n}{\Delta t},$$

where superscripts denote time levels.

Substituting the discretized derivatives into the PDEs, we obtain the finite-difference equations:

$$\frac{u_{i,j}^{n+1} - u_{i,j}^n}{\Delta t} = f(u_{i,j}^n, v_{i,j}^n) + D_u \frac{u_{i+1,j}^n + u_{i-1,j}^n + u_{i,j+1}^n + u_{i,j-1}^n - 4u_{i,j}^n}{\Delta x^2},$$
$$\frac{v_{i,j}^{n+1} - v_{i,j}^n}{\Delta t} = g(u_{i,j}^n, v_{i,j}^n) + D_v \frac{v_{i+1,j}^n + v_{i-1,j}^n + v_{i,j+1}^n + v_{i,j-1}^n - 4v_{i,j}^n}{\Delta x^2}.$$

Rearranging these equations gives the update formulas for u and v at each time step.

The stability of the explicit finite-difference scheme is crucial. For nonlinear systems like Turing patterns the time step Δt must be chosen carefully relative to the spatial discretization Δx to ensure stability. The diffusion terms typically impose a restriction of the form $\Delta t \propto \Delta x^2/D$, where D is the diffusion coefficient.

The truncation error in the finite-difference approximation is of order $O(\Delta x^2)$ for the spatial derivatives and $O(\Delta t)$ for the time derivative.

References

Philip K Maini. Using mathematical models to help understand biological pattern formation. *Comptes rendus. Biologies*, 327(3):225–234, 2004.

Alan M Turing. The chemical basis of morphogenesis. *Philosophical Transactions of the Royal Society of London. Series B, Biological Sciences*, 237(641):37–72, 1952.

Alfred Gierer and Hans Meinhardt. A theory of biological pattern formation. *Kybernetik*, 12:30–39, 1972.

Michael F. Staddon. How the zebra got its stripes: Curvature-dependent diffusion orients turing patterns on three-dimensional surfaces. *Physical Review E*, 110(3):034402, 2024. doi: 10.1103/PhysRevE.110.034402.

Shigeru Kondo, Masakatsu Watanabe, and Seita Miyazawa. Studies of turing pattern formation in zebrafish skin. *Philosophical Transactions of the Royal Society A: Mathematical, Physical and Engineering Sciences*, 379(2216):20200274, 2021. doi: 10.1098/rsta.2020.0274. URL `https://doi.org/10.1098/rsta.2020.0274`.

Akiko Nakamasu, Go Takahashi, Akio Kanbe, and Shigeru Kondo. Interactions between zebrafish pigment cells responsible for the generation of turing patterns. *Proceedings of the National Academy of Sciences*, 106(21):8429–8434, 2009. doi: 10.1073/pnas.0808622106.

Ebrahim Jahanbakhsh and Michel C. Milinkovitch. Modeling convergent scale-by-scale skin color patterning in multiple species of lizards. *Current Biology*, 32(23):R1306–R1308, 2022. doi: 10.1016/j.cub.2022.10.044.

P.K. Maini and T.E. Woolley. The turing model for biological pattern formation. In A. Bianchi, T. Hillen, M. Lewis, and Y. Yi, editors, *The Dynamics of Biological Systems*, volume 4 of *Mathematics of Planet Earth*. Springer, Cham, 2019. doi: 10.1007/978-3-030-22583-4_7. URL `https://doi.org/10.1007/978-3-030-22583-4_7`.

Benjamin M. Alessio and Ankur Gupta. Diffusiophoresis-enhanced turing patterns. *Science Advances*, 9(45):adj2457, Nov 2023. doi: 10.1126/sciadv.adj2457. URL `https://doi.org/10.1126/sciadv.adj2457`.

A. Diez, A.L. Krause, P.K. Maini, E.A. Gaffney, and S. Seirin-Lee. Exploring turing pattern formation in reaction-cross-diffusion models: Stability effects of growth terms and scaling mechanisms for pattern coherence. *bioRxiv*, 2023. URL `https://www.biorxiv.org/content/10.1101/2023.05.30.542795.pdf`.

S. Werner, T. Stückemann, M. Beirán Amigo, and J.C. Rink. Scaling and regeneration of self-organized turing patterns under feedback mechanisms and environmental perturbations. *arXiv*, 2015. URL `https://arxiv.org/pdf/1411.2359`.

Y. Benenson. Challenges in integrating turing-like patterns in biomolecular computing systems: Complexity in representing biological processes and molecular machines. *Nature Reviews Genetics*, 2012. URL `https://www.nature.com/articles/nrg3197`.

M. Tanaka, S.M. Montgomery, L. Yue, et al. Framework for applying turing patterns in synthetic biology: Streamlined data integration to retain fidelity across biological scales. *Science Advances*, 2023. URL `https://www.science.org/doi/abs/10.1126/sciadv.ade4381`.

A. Volkening. Survey on self-organization quantification and the integration of turing patterns in stochastic biological systems. *arXiv*, 2024. URL https://arxiv.org/pdf/2407.10832.

S. Kondo. Updated turing model for biological pattern formation: Addressing limitations in reaction-diffusion models for specific biological environments. *Journal of Theoretical Biology*, 2017. URL https://www.sciencedirect.com/science/article/pii/S0022519316303630.

A.L. Krause and E.A. Gaffney. Advances in turing's morphogenesis theory: Adapting models to complex biological dynamics. *Philosophical Transactions of the Royal Society A*, 2021. URL https://royalsocietypublishing.org/doi/abs/10.1098/rsta.2020.0280.

M. Rietkerk et al. Spatial pattern formation in ecological systems: Challenges of turing model adaptation to large-scale dynamics. *Science*, 2021. URL https://research.rug.nl/files/193917119/science.abj0359.pdf.

Michel C Milinkovitch, Ebrahim Jahanbakhsh, and Szabolcs Zakany. The unreasonable effectiveness of reaction diffusion in vertebrate skin color patterning. *Annual Review of Cell and Developmental Biology*, 39:145–174, 2023. doi: 10.1146/annurev-cellbio-120319-024414. URL https://doi.org/10.1146/annurev-cellbio-120319-024414.

D. Schnoerr, E. Tonello, T. Leyshon, and H. Siebert. The design principles of discrete turing patterning systems. *bioRxiv*, October 2020. doi: 10.1101/2020.10.18.344135. URL https://www.biorxiv.org/content/10.1101/2020.10.18.344135. License: CC BY-NC 4.0.

T.E. Woolley, A.L. Krause, and E.A. Gaffney. Bespoke turing systems: Focusing on parameter stability and maintaining robust patterns in variable environments. *Bulletin of Mathematical Biology*, 2021. URL https://link.springer.com/content/pdf/10.1007/s11538-021-00870-y.pdf.

Luciano Marcon, Xavier Diego, James Sharpe, and Patrick Müller. High-throughput mathematical analysis identifies turing networks for patterning with equally diffusing signals. *eLife*, 5:e14022, 04 2016. doi: 10.7554/eLife.14022. URL https://doi.org/10.7554/eLife.14022.

Xavier Diego, Luciano Marcon, Patrick Müller, and James Sharpe. Key features of turing systems are determined purely by network topology. *Physical Review X*, 8(2):021071, 2018. doi: 10.1103/PhysRevX.8.021071.

Natalie S Scholes, David Schnoerr, Mark Isalan, and Michael P H Stumpf. A comprehensive network atlas reveals that turing patterns are common but not robust. *Cell Systems*, 9(3): 243–257.e4, 2019. doi: 10.1016/j.cels.2019.07.007. URL https://www.sciencedirect.com/science/article/pii/S2405471219302649.

Ushasi Roy, Divyoj Singh, Navin Vincent, Chinmay K Haritas, and Mohit Kumar Jolly. Spatiotemporal patterning enabled by gene regulatory networks. *ACS Omega*, 8(4):3713–3725, 2023. doi: 10.1021/acsomega.2c04581. URL https://doi.org/10.1021/acsomega.2c04581.

Mohit P Dalwadi and Philip Pearce. Universal dynamics of biological pattern formation in spatio-temporal morphogen variations. *Proceedings of the Royal Society A*, 479(2271): 20220829, 2023.

Sean T Vittadello, Thomas Leyshon, David Schnoerr, and Michael P H Stumpf. Turing pattern design principles and their robustness. *Philosophical Transactions of the Royal Society A: Mathematical, Physical and Engineering Sciences*, 378(2189):20200272, 2020.

Jure Tica, Martina Oliver Huidobro, Tong Zhu, Georg KA Wachter, Roozbeh H. Pazuki, Elisa Tonello, Heike Siebert, Michael PH Stumpf, Robert G Endres, and Mark Isalan. A three-node turing gene circuit forms periodic spatial patterns in bacteria. *bioRxiv*, pages 2023–10, 2023.

Václav Klika. Significance of non-normality-induced patterns: Transient growth versus asymptotic stability. *Chaos: An Interdisciplinary Journal of Nonlinear Science*, 27(7): 073120, 2017. doi: 10.1063/1.4985256. URL https://doi.org/10.1063/1.4985256.

EA; Jewell-TJ; Klika V; Walker BJ Krause, AL; Gaffney. Turing instabilities are not enough to ensure pattern formation. *Bulletin of Mathematical Biology*, 86(21), 2024. doi: 10.1007/s11538-023-01250-4.

Yanyan Chen and Javier Buceta. A non-linear analysis of turing pattern formation. *PLoS ONE*, 14(8):e0220994, 08 2019. doi: 10.1371/journal.pone.0220994. URL https://doi.org/10.1371/journal.pone.0220994.

J. L. Aragón, R. A. Barrio, T. E. Woolley, R. E. Baker, and P. K. Maini. Nonlinear effects on turing patterns: Time oscillations and chaos. *Phys. Rev. E*, 86(2):026201, 2012. doi: 10.1103/PhysRevE.86.026201. URL https://doi.org/10.1103/PhysRevE.86.026201.

Martina Oliver Huidobro and Robert G. Endres. Effects of multistability, absorbing boundaries and growth on turing pattern formation. *bioRxiv*, 2024. doi: 10.1101/2024.09.09.611947. URL https://doi.org/10.1101/2024.09.09.611947.

Roozbeh H. Pazuki and Robert G. Endres. Robustness of turing models and gene regulatory networks with a sweet spot. *Phys. Rev. E*, 109:064305, 2024. doi: 10.1103/PhysRevE.109.064305. URL https://doi.org/10.1103/PhysRevE.109.064305.

Shibashis Paul, Joy Adetunji, and Tian Hong. Widespread biochemical reaction networks enable turing patterns without imposed feedback. *Nature Communications*, 14, 2023.

Jasper van der Kolk, Guillermo García-Pérez, Nikos E. Kouvaris, M. Ángeles Serrano, and Marián Boguñá. Emergence of geometric turing patterns in complex networks. *Physical Review X*, 13(021038), 2023. doi: 10.1103/PhysRevX.13.021038.

Ajay Subbaroyan, Olivier C. Martin, and Areejit Samal. Minimum complexity drives regulatory logic in boolean models of living systems. *PNAS Nexus*, 1(1):pgac017, 2022. doi: 10.1093/pnasnexus/pgac017.

Pascal F. Hagolani, Roland Zimm, Renske Vroomans, and Isaac Salazar-Ciudad. On the evolution and development of morphological complexity: A view from gene regulatory networks. *Journal of Theoretical Biology*, 2023.

Saverio Forestiero. The historical nature of biological complexity and the ineffectiveness of the mathematical approach to it. *Acta Biotheoretica*, 2022. doi: 10.1007/s12064-022-00369-7.

J. S. McGough and K. Riley. Pattern formation in the gray–scott model. *Nonlinear Analysis: Real World Applications*, 5(1):105–121, 2004. doi: 10.1016/S1468-1218(03)00020-8.

P. Gray and S. K. Scott. Autocatalytic reactions in the isothermal, continuous stirred tank reactor: isolas and other forms of multistability. *Chemical Engineering Science*, 38(1): 29–43, 1983. doi: 10.1016/0009-2509(83)80194-7.

S. Li M. Zheng and B. Xu. High-fidelity simulations for turing pattern formation in multidimensional gray-scott reaction-diffusion system. *Computers & Mathematics with Applications*, 80(7):1611–1621, 2020. doi: 10.1016/j.camwa.2020.07.020.

Q. Yang J. Li and Y. Zhang. Uniform patterns formation based on gray-scott model for 3d printing. *Journal of Applied Mathematics and Physics*, 7(12):2884–2895, 2019. doi: 10.4236/jamp.2019.712198.

Alan Hodgkin and Andrew Huxley. A quantitative description of membrane current and its application to conduction and excitation in nerve. *J. Physiol.*, 117(4):500–544, 1952.

Richard FitzHugh. Impulses and physiological states in theoretical models of nerve membrane. *Biophys. J.*, 1(6):445–466, 1961.

Suguru Arimoto Jinichi Nagumo and Shuji Yoshizawa. An active pulse transmission line simulating nerve axon. *Proc. IRE*, 50(10):2061–2070, 1962.

Daniel Ruiz-Reynes Daniel Cebrian-Lacasa, Pedro Parra-Rivas and Lendert Gelens. Six decades of the fitzhugh-nagumo model: A guide through its spatio-temporal dynamics and influence across disciplines. *arXiv preprint arXiv:2404.11403*, 2024. URL `https://arxiv.org/abs/2404.11403`.

Gaetana Gambino, Maria Cristina Lombardo, Gino Rubino, and Marcello Sammartino. Pattern selection in the 2d fitzhugh–nagumo model. *Ricerche di Matematica*, 67(2):377–392, 2018. doi: 10.1007/s11587-018-0424-6.

Ben D MacArthur, Avi Ma'ayan, and Ihor R Lemischka. Systems biology perspectives on stem cell fate. *Nature Reviews Molecular Cell Biology*, 10(9):672–681, 2009.

Johan Paulsson. Summing up the noise in gene networks. *Nature*, 427(6973):415–418, 2004.

Imke Roeder and Ingmar Glauche. Modeling stem cell behavior with bayesian inference. *Nature*, 441:435, 2006.

J Lynn Cherry and Frederick R Adler. How to make a biological switch. *Journal of Theoretical Biology*, 203(2):117–133, 2000.

Understanding gene circuits at cell-fate branch points for rational cell reprogramming. *Trends in Genetics*, 27(2):55–62, 2011. ISSN 0168-9525. doi: https://doi.org/10.1016/j.tig.2010.11.002.

Ruben Perez-Carrasco, Pilar Guerrero, James Briscoe, and Karen Page. Intrinsic noise profoundly alters the dynamics and steady state of morphogen-controlled bistable genetic switches. *PLoS Computational Biology*, 12(8):e1005154, 2016.

Patrick B Warren and Pieter Rein ten Wolde. Statistical analysis of the spatial patterns of cell-to-cell communication. *Journal of Computational Biology*, 11(2-3):308–325, 2004.

Thomas B Kepler and Timothy C Elston. Stochasticity in transcriptional regulation: origins, consequences, and mathematical representations. *Biophysical Journal*, 81(6):3116–3136, 2001.

Vijay Chickarmane, Tariq Enver, and Carsten Peterson. A bistable switch in myeloid differentiation. *Journal of Theoretical Biology*, 244(1):68–76, 2006.

Michael K Strasser, Fabian J Theis, and Carsten Marr. Stability and multi-attractor dynamics of a toggle switch based on a two-stage model of stochastic gene expression. *Biophysical Journal*, 101(3):611–621, 2011.

Ming-Chang Huang, Jinn-Wen Wu, Yu-Pin Luo, and Karen G Petrosyan. Fluctuations in gene regulatory networks as gaussian colored noise. *Journal of Chemical Physics*, 130(14):145101, 2009.

Makoto Sato, Tetsuo Yasugi, Yoshiaki Minami, and Masaharu Nagayama. Notch-mediated lateral inhibition regulates proneural wave propagation when combined with egf-mediated reaction diffusion. *Proceedings of the National Academy of Sciences*, 113(35):E5153–E5162, August 2016. doi: 10.1073/pnas.1602739113. URL `https://doi.org/10.1073/pnas.1602739113`.

Adamatzky A and Costello BDL. *Reaction–Diffusion Computing*, pages 1897–1920. Springer Berlin Heidelberg, Berlin, Heidelberg, 2012. ISBN 978-3-540-92910-9. doi: 10.1007/978-3-540-92910-9_56. URL `https://doi.org/10.1007/978-3-540-92910-9_56`.